Quasicylindrical description of a swirling light gas jet discharging into a heavier ambient gas

J. M. Gallardo-Ruiz, C. del Pino, and R. Fernandez-Feria
E. T. S. Ingenieros Industriales, Universidad de Málaga, Dr Ortiz Ramos s/n, 29071 Málaga, Spain

(Received 12 April 2010; accepted 3 August 2010; published online 1 November 2010)

The structure of an axisymmetric swirling gas jet of a light species discharging into an ambient of a heavier gas is analyzed using the quasicylindrical approximation of the compressible flow equations, with the main aim of describing the conditions for the onset of vortex breakdown. A self-similar solution valid in the mixing-layer close to the jet exit is found, which is used to start the numerical integration of the parabolic equations. For the computations, we consider the particular case of a swirling jet of hydrogen discharging into air. We characterize the critical swirl number for vortex breakdown as a function of the coflow velocity of the ambient gas, and compare it to the case of a homogeneous, single-species gas jet, discussing the physical differences found between the cases. We also consider the influence of the Mach number on the onset of vortex breakdown, and discuss the results in relation to the incompressible limit, finding that the swirl level for breakdown decreases as the Mach number increases.
[doi:10.1063/1.3489127]

I. INTRODUCTION

Swirling jets occur in many engineering applications. A distinctive feature of these vortex flows is the appearance of the so-called vortex breakdown (VB) phenomenon above a certain swirl intensity level (see, e.g., Ref. 1). Although there exists a large body of information on the breakdown of incompressible and homogeneous swirling jets, both theoretical/numerical (e.g., Refs. 2–5) and experimental,[6–10] much less is known about VB in swirling jets of a light molecular species discharging into an ambient gas constituted by a heavier molecular species. These light gas swirling jets (LGSJs) are relevant, for instance, in combustion processes, where in many circumstances the fuel is a light species, such as H_2, which is injected into an ambient of an oxidant gas, such as O_2 or air, whose molecules are much heavier. In addition, vortex breakdown is an important phenomenon in combustion systems, which is searched for flame stabilization, to enhance mixing and reduce pollution.[11,12] In most swirl combustors, however, the injected oxidizer rotates while the fuel does not,[13] in opposition to the configuration considered here; in addition, the flow is usually turbulent, while we consider a laminar flow. However to gain further theoretical understanding of the flow conditions for the onset of VB in these combustion systems, and in other hydrogen or helium, jet applications where swirl is used to enhance mixing, it is of interest to characterize the onset of VB in these LGSJs, and analyze the differences in relation to a homogeneous (single-species) and incompressible swirling jet.

This is the objective of the present work, which we undertake by solving the quasicylindrical (QC) approximation[14] of the equations governing the axisymmetric and compressible jet flow, valid for high Reynolds numbers. Although it is well known that this approximation ceases to be valid after the flow undergoes VB, it is a useful approximation to predict the critical swirl intensity for the onset of VB, which corresponds to the failure of the QC approximation.[4,15–18] In our analysis we include the compressibility effects on the LGSJ structure, and characterize the dependence of the onset of VB on the Mach number of the jet. There exists a number of works which analyze the effect of compressibility on the breakdown of several types of vortex flows (e.g., Refs. 17 and 19–22), but the study of compressibility effects on the VB onset in LGSJ, or even in swirling jets in general, is novel to our knowledge. We also include in the analysis presented here the effect of the coflow velocity of the ambient gas, which is also very relevant in combustion processes. No chemical reactions are, however, considered in this work, in which we are interested in the subsonic flow structure described by the QC approximation.

The structure of the paper is the following: After formulating the problem in the next section, a self-similar solution valid for the mixing-layer close to the jet exit is given in Sec. III. This solution is used in the following section to start the numerical integration of the QC equations. In that section the numerical method is introduced and validated against known analytical solutions, and the numerical results for the different cases considered are presented and discussed. This paper ends with a conclusions section.

II. FORMULATION OF THE PROBLEM

A. General formulation

We consider the discharge of a swirling gas jet through a pipe of radius R_I into an ambient gas. For simplicity, we consider only two chemical species, the one introduced with the swirling jet (the *fuel*, which will be a light molecular species such as H_2), with a mass fraction denoted by Y, and that in the ambient gas where the jet discharges (the *oxidant* or heavy molecular species, such as O_2 or air), with mass fraction given by $1-Y$. Chemical reactions will be neglected.

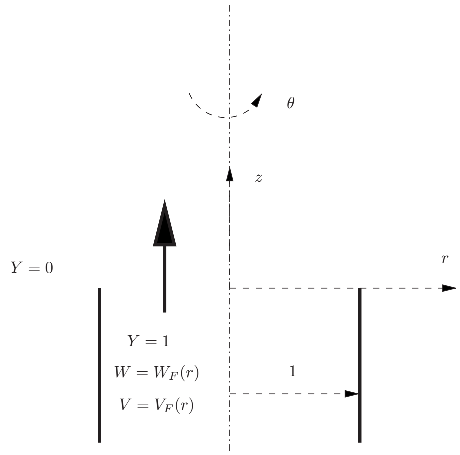

FIG. 1. Sketch of the dimensionless geometry and boundary conditions at $z=0$.

We use cylindrical polar coordinates (r,θ,z). The jet enters at $z=0$ with $Y=1$ (pure fuel) through the orifice of radius R_I, which is used as a characteristic radius to render dimensionless the radial coordinate r (see Fig. 1). The axial coordinate z is made dimensionless by scaling it with characteristic axial length z_c, to be defined below, in such a way that the dimensional position vector $\mathbf{x}$ is related to the nondimensional cylindrical coordinates (r,θ,z) through

$$\mathbf{x}=\left(R_I r,\theta,\frac{R_I}{\delta}z\right),\qquad \delta\equiv\frac{R_I}{z_c}. \tag{1}$$

To define the remaining dimensionless variables we scale them with their corresponding characteristic values at the fuel inlet. However it is important to note first that we shall consider the limit of high Reynolds number of the jet, defined as

$$\mathrm{Re}=\frac{W_c R_I \rho_{Fc}}{\mu_{Fc}}, \tag{2}$$

where W_c is a characteristic axial velocity of the incoming jet at $z=0$, and ρ_{Fc} and μ_{Fc} are characteristic values of the density and viscosity, respectively, of the fuel species at the (inlet) reference temperature T_c. In the limit $\mathrm{Re}\gg 1$, corresponding to the quasicylindrical approximation, where the characteristic axial length z_c is much larger than the characteristic radius R_I, we may choose, without loss of generality and for the sake of simplicity,

$$z_c=\mathrm{Re}\,R_I \quad\text{or}\quad \delta^{-1}=\mathrm{Re}, \tag{3}$$

eliminating the scaling factor δ and, therefore, the Reynolds number from the QC formulation (see below).

The nondimensional order unity velocity field (U,V,W) is defined, in terms of the dimensional velocity field $\mathbf{v}$, as

$$\mathbf{v}=W_c\begin{pmatrix}\delta U\\ V\\ W\end{pmatrix}, \tag{4}$$

where it has been taken into account that from the continuity equation, the radial velocity of the jet is not of the order W_c like the axial velocity, but of the order δW_c.

We assume a perfect gas equation of state for the mixture, relating the density ρ to the pressure p, the temperature T, and the mass fraction Y by

$$\rho=\frac{p}{RT}\frac{1}{\dfrac{Y}{M_F}+\dfrac{1-Y}{M_O}}=\frac{M_F}{R}\frac{p}{T}\frac{1}{Y+\epsilon(1-Y)},\qquad \epsilon\equiv\frac{M_F}{M_O}, \tag{5}$$

where $R\simeq 8.314\ \mathrm{J\,mol^{-1}\,K^{-1}}$ is the universal molar gas constant, and M_F and M_O are the molecular weights of the fuel and oxidant species, respectively. The ratio of molecular weights ϵ will be a small parameter in the LGSJ case considered in this work, although the problem is formulated here for arbitrary values of ϵ. The nondimensional density ϱ, pressure P, and temperature Θ are defined in terms of their dimensional counterparts ρ, p, and T as

$$\rho=\rho_{Fc}\varrho,\quad p=p_c P,\quad T=T_c\Theta, \tag{6}$$

where the characteristic pressure is given by $p_c=\rho_{Fc}\times RT_c/M_F$.

For the viscosity and thermal conductivity of the mixture, μ and K, we shall use the semiempirical expressions[23]

$$\mu=\mu_F\frac{Y+\epsilon^{1/2}(1-Y)\dfrac{\mu_O}{\mu_F}}{Y+\epsilon^{1/2}(1-Y)}, \tag{7}$$

$$K=K_F\frac{Y+\epsilon^{2/3}(1-Y)\dfrac{K_O}{K_F}}{Y+\epsilon^{2/3}(1-Y)}, \tag{8}$$

respectively, where μ_F and μ_O are the viscosity coefficients and K_F and K_O are the thermal conductivities of the fuel and oxidant species, respectively, all of them functions of the temperature.

Assuming that the flow is axisymmetric and steady (i.e., the flow magnitudes only depend on r and z), and neglecting terms of the order of $\delta^2=\mathrm{Re}^{-2}$ (QC approximation) in the compressible flow equations, the problem is governed by the following nondimensional system of equations:

$$\frac{1}{r}\frac{\partial}{\partial r}(r\varrho U)+\frac{\partial}{\partial z}(\varrho W)=0, \tag{9}$$

$$\varrho U\frac{\partial Y}{\partial r}+\varrho W\frac{\partial Y}{\partial z}=\frac{1}{r}\frac{\partial}{\partial r}\left(\frac{r\varrho}{\mathrm{Sc}}\frac{\partial Y}{\partial r}\right), \tag{10}$$

$$\varrho=\frac{P}{\Theta}\frac{1}{Y+\epsilon(1-Y)}, \tag{11}$$

$$\varrho\frac{V^2}{r}=E\frac{\partial P}{\partial r}, \tag{12}$$

$$\varrho\left(U\frac{\partial V}{\partial r}+\frac{UV}{r}+W\frac{\partial V}{\partial z}\right)=\frac{1}{r^2}\frac{\partial}{\partial r}\left(r^3\mu\frac{\partial(V/r)}{\partial r}\right), \tag{13}$$

$$\varrho\left(U\frac{\partial W}{\partial r}+W\frac{\partial W}{\partial z}\right)=-E\frac{\partial P}{\partial z}-\frac{1}{\mathrm{Fr}}\varrho+\frac{1}{r}\frac{\partial}{\partial r}\left(r\mu\frac{\partial W}{\partial r}\right), \tag{14}$$

$$\varrho\left(U\frac{\partial \Theta}{\partial r}+W\frac{\partial \Theta}{\partial z}\right)=\alpha_F\frac{\gamma-1}{\gamma}\left(U\frac{\partial P}{\partial r}+W\frac{\partial P}{\partial z}\right)+\frac{\alpha_F}{\mathrm{Pr}}\frac{1}{r}\frac{\partial}{\partial r}\left(rK\frac{\partial \Theta}{\partial r}\right)+\frac{\alpha_F-\alpha_O}{\mathrm{Sc}}\varrho\frac{\partial \Theta}{\partial r}\frac{\partial Y}{\partial r}. \tag{15}$$

Equation (9) is the continuity equation of the mixture. In the fuel mass conservation equation (10) we have neglected thermal diffusion (and, of course, chemical reactions), and the Schmidt number is defined as

$$\mathrm{Sc}=\frac{\mu_{Fc}}{\rho_{Fc}D}, \tag{16}$$

where D is the coefficient of binary diffusion between both species. Equation (11) is the equation of state for the mixture. Equations (12)–(14) are the radial, azimuthal, and axial components, respectively, of the momentum equation for the mixture, where we have neglected compressibility effects in the viscous forces, although, of course, compressibility effects are taken into account everywhere else. E is an Euler number, related to the Mach number Ma of the jet and to the fuel specific-heat ratio γ through

$$E=\frac{p_c}{\rho_{Fc}W_c^2}=\frac{1}{\gamma\,\mathrm{Ma}^2},\quad \mathrm{Ma}^2=\frac{W_c^2}{\gamma p_c/\rho_{Fc}},\quad \gamma=\frac{c_{pF}}{c_{vF}}. \tag{17}$$

In the axial component (14) we have included, for completeness, the gravitational forces in the z direction, with acceleration g, and the Froude number is defined as

$$\mathrm{Fr}=\frac{W_c^2}{z_c g}=\frac{W_c^2}{R_I g}\frac{1}{\mathrm{Re}}. \tag{18}$$

Finally, Eq. (15) is the energy equation of the mixture, where we have neglected the viscous dissipation term as well as the Dufour effect in the heat flux [consequently with neglecting thermal diffusion in Eq. (10)], and we have assumed that the mixture specific heat at constant pressure, $c_p=Yc_{pF}+(1-Y)c_{pO}$, is constant. We have defined the Prandtl number as

$$\mathrm{Pr}=\frac{c_{pF}\mu_{Fc}}{K_{Fc}} \tag{19}$$

and the specific-heat ratios as

$$\alpha_F=\frac{c_{pF}}{c_p},\quad \alpha_O=\frac{c_{pO}}{c_p}. \tag{20}$$

In addition, to simplify the notation, we have used in Eqs. (13)–(15) the same letters to denote the dimensionless viscosity and heat conductivity of the mixture, scaled with the corresponding characteristic values for the fuel species,

$$\mu\leftarrow\frac{\mu}{\mu_{Fc}},\quad K\leftarrow\frac{K}{K_{Fc}}. \tag{21}$$

We are interested in solving Eqs. (9)–(15) with the following inlet boundary conditions at $z=0$ (see Fig. 1):

$$U=0,\quad W=W_F(r),\quad V=SV_F(r),\quad Y=1,\qquad \Theta=1,\quad \text{at } z=0 \quad \text{for } 0\le r\le 1, \tag{22}$$

$$U=0,\quad W=\bar{W}_O(r),\quad V=0,\quad Y=0,\qquad \Theta=1,\quad \text{at } z=0 \quad \text{for } r>1, \tag{23}$$

where W_F, V_F, and $\bar{W}_O$ are given functions of r of order unity, and S is a swirl number, the last of the series of nondimensional parameters governing the structure of the flow described here (but the most relevant one in the present work), defined as the ratio between a characteristic azimuthal velocity V_c and W_c,

$$S=\frac{V_c}{W_c}. \tag{24}$$

The pressure is not specified in Eqs. (22) and (23) because it can be obtained from $V_F(r)$ through the radial momentum equation (12) together with a given reference value (say, $P\to P_O$ as $r\to\infty$). On the other hand, the density ϱ at $z=0$ is computed from the equation of state (11).

The remaining boundary conditions for the parabolic equations (9)–(15) are the symmetry condition at the axis $r=0$,

$$\frac{\partial Y}{\partial r}=\frac{\partial W}{\partial r}=\frac{\partial \Theta}{\partial r}=U=V=0\quad \text{at } r=0\quad \text{for } z>0, \tag{25}$$

and the given external values of Y, V, W, P, and Θ as $r\to\infty$,

$$Y\to 0,\quad V\to 0,\quad W\to W_O,\quad P\to P_O,\qquad \Theta\to 1,\quad \text{as } r\to\infty, \tag{26}$$

for given constants W_O and P_O.

B. Simplified equations for a light jet emerging with uniform axial velocity and rotating as a rigid body

We consider in this work the simplest case where Sc, μ_F, and K_F are constants, $\alpha_F=\alpha_O=1$ (i.e., $c_{pF}=c_{pO}=c_p$), and buoyancy (Froude number) effects are negligible. In the case of a jet constituted by a gas much lighter than the ambient ($\epsilon\ll 1$), the mixture viscosity and heat conductivity may be assumed constants, according to Eqs. (7) and (8), at the lowest order in ϵ. Since μ and K are made dimensionless with the characteristic values of the jet species [Eq. (21)], we can write $\mu\simeq K\simeq 1$ in Eqs. (13)–(15). Note that this is also valid for the particular case of a constant-density (single-species) jet problem ($\epsilon=1$ and $Y=1$ everywhere) so that the resulting equations given below can be used in both cases, $\epsilon=1$ and $\epsilon\ll 1$, which is of special interest for comparing the LGSJ results with the constant-density swirling jet results.

Using the above approximations, Eqs. (9)–(15) can be rewritten as

$$\frac{1}{r}\frac{\partial}{\partial r}(r\varrho U)+\frac{\partial}{\partial z}(\varrho W)=0, \tag{27}$$

$$\varrho U\frac{\partial Y}{\partial r}+\varrho W\frac{\partial Y}{\partial z}=\frac{\mathrm{Sc}^{-1}}{r}\frac{\partial}{\partial r}\left(r\varrho\frac{\partial Y}{\partial r}\right), \tag{28}$$

$$\varrho=\frac{\gamma\,\mathrm{Ma}^2\;\bar{P}+1}{\Theta}\frac{1}{Y+\epsilon(1-Y)}, \tag{29}$$

$$\varrho\frac{V^2}{r}=\frac{\partial\bar{P}}{\partial r}, \tag{30}$$

$$\varrho\left(U\frac{\partial V}{\partial r}+\frac{UV}{r}+W\frac{\partial V}{\partial z}\right)=\frac{1}{r^2}\frac{\partial}{\partial r}\left(r^3\frac{\partial(V/r)}{\partial r}\right), \tag{31}$$

$$\varrho\left(U\frac{\partial W}{\partial r}+W\frac{\partial W}{\partial z}\right)=-\frac{\partial\bar{P}}{\partial z}+\frac{1}{r}\frac{\partial}{\partial r}\left(r\frac{\partial W}{\partial r}\right), \tag{32}$$

$$\varrho\left(U\frac{\partial\Theta}{\partial r}+W\frac{\partial\Theta}{\partial z}\right)=(\gamma-1)\mathrm{Ma}^2\left(U\frac{\partial\bar{P}}{\partial r}+W\frac{\partial\bar{P}}{\partial z}\right)+\frac{\mathrm{Pr}^{-1}}{r}\frac{\partial}{\partial r}\left(r\frac{\partial\Theta}{\partial r}\right). \tag{33}$$

Note that we have redefined the nondimensional pressure as

$$\bar{P}\equiv E(P-1)=\frac{P-1}{\gamma\,\mathrm{Ma}^2} \tag{34}$$

so that Ma (or E) disappears from the momentum equations (12)–(14), with $\bar{P}$ replacing P, but appearing in the equation of state (11) and the energy equation (15). This formulation is clearly more appropriate if one has to consider the incompressible limit $\mathrm{Ma}\to 0$, which corresponds to $E\to\infty$. Implicit in Eq. (34) is that the nondimensional reference pressure is, without loss of generality, $P_O=1$.

In addition we assume a uniform inlet flow, with the jet rotating as a rigid body so that the boundary conditions (22) and (23) at $z=0$ become

$$U=0,\quad \Theta=1, \tag{35}$$

$$W=\begin{cases}1 & \text{for } 0\le r\le 1\\ W_O & \text{for } r>1,\end{cases} \tag{36}$$

$$V=\begin{cases}Sr & \text{for } 0\le r\le 1\\ 0 & \text{for } r>1,\end{cases} \tag{37}$$

$$Y=\begin{cases}1 & \text{for } 0\le r\le 1\\ 0 & \text{for } r>1,\end{cases} \tag{38}$$

where the coflow W_O is a known constant. From Eqs. (29) and (30) and Eqs. (35)–(38) the pressure and density profiles at $z=0$ are given by

$$\bar{P}=\begin{cases}\dfrac{1}{\gamma\,\mathrm{Ma}^2}(e^{S^2\gamma\,\mathrm{Ma}^2(r^2-1)/2}-1) & \text{for } 0\le r\le 1\\ 0 & \text{for } r>1,\end{cases} \tag{39}$$

$$\varrho=\begin{cases}e^{S^2\gamma\,\mathrm{Ma}^2(r^2-1)/2} & \text{for } 0\le r\le 1\\ \epsilon^{-1} & \text{for } r>1.\end{cases} \tag{40}$$

In the incompressible limit ($\mathrm{Ma}^2=0$), the last two boundary conditions become

$$\bar{P}=\begin{cases}\dfrac{S^2(r^2-1)}{2} & \text{for } 0\le r\le 1\\ 0 & \text{for } r>1,\end{cases} \tag{41}$$

$$\varrho=\begin{cases}1 & \text{for } 0\le r\le 1\\ \epsilon^{-1} & \text{for } r>1.\end{cases} \tag{42}$$

The remaining boundary conditions are the same as Eqs. (25) and (26), except for $\bar{P}\to 0$ as $r\to\infty$.

This simplified problem is thus governed by the dimensionless parameters S, ϵ, Sc, Ma, γ, Pr, and W_O. We shall vary the swirl parameter S, the coflow W_O, and the Mach number Ma, keeping the remaining parameters constant for a given gas mixture (e.g., hydrogen-air, $\epsilon=0.07$) or a homogeneous jet ($\epsilon=1$).

III. SELF-SIMILAR SOLUTION NEAR $z=0$

In the absence of swirl ($V=0$), the problem is governed by just Eqs. (27), (28), and (32), with $\bar{P}=0$ and $\Theta=1$ everywhere because there is no rotation to generate pressure differences through Eq. (30) and, therefore, temperature gradients in the jet. This nonswirling problem was considered by Sánchez-Sanz *et al.*,[24] finding that for a uniform axial velocity profile at the jet inlet, the problem admits a self-similar solution near the jet exit (i.e., for $z\ll 1$ and $|r-1|\ll 1$), in terms of the self-similar variable

$$\eta=\frac{r-1}{\sqrt{z}}, \tag{43}$$

which describes a slender mixing-layer between the jet and the ambient gas in the vicinity of the orifice rim $r=1$ close to $z=0$. This is the same self-similar variable that describes the planar mixing-layer.[25]

When $V\neq 0$ and given by solid body rotation at the jet inlet, the problem still admits a self-similar solution for $z\ll 1$ in terms of variable (43), as does the incompressible, single-species counterpart analyzed by Revuelta *et al.*[4] As we shall see below, the introduction of swirl does not affect the self-similar solution of the problem without swirl at its lowest order, entering as a correction in the next order $[O(\sqrt{z})]$.

In effect, boundary conditions (35) and (39), together with Eqs. (30) and (29), suggest the introduction of the following self-similar dependence for $\bar{P}$, V, and Θ at the lowest order in $z\ll 1$:

$$\bar{P}=\sqrt{z}P_1(\eta), \tag{44}$$

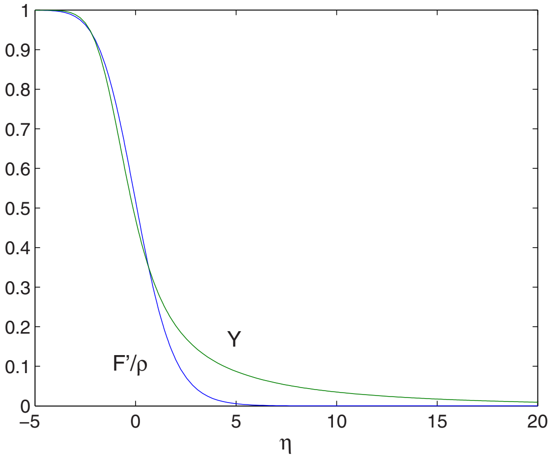

FIG. 2. (Color online) Axial velocity $W=F'/\varrho$ and mass fraction Y as functions of η for $S_c=1.39$, $\epsilon=0.07$ (corresponding to hydrogen-air), and $W_O=0$. The numerical integration was performed between $-20\leq\eta\leq 50$.

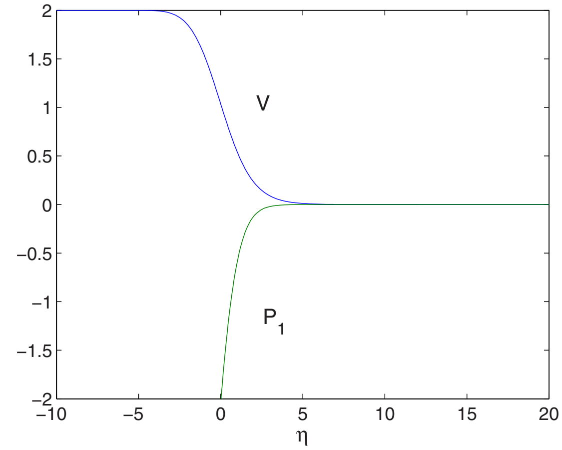

FIG. 3. (Color online) Tangential velocity V and pressure correction P_1 as functions of η for $S=2$, and the same remaining parameters used in Fig. 2.

$$V=V(\eta), \tag{45}$$

$$\Theta=1+\sqrt{z}\Theta_1(\eta). \tag{46}$$

The rest of the flow variables remain unchanged, at the lowest order, in relation to the swirless and incompressible flow. In terms of the stream function Ψ, which simplifies the analysis by automatically satisfying continuity equation (27), the self-similar solution at the lowest order in $\sqrt{z}$, close to $r=1$, can be expressed as[24]

$$\Psi=\sqrt{z}F(\eta), \quad \varrho W=\frac{\partial\Psi}{\partial r}=F',$$
$$\varrho U=-\frac{\partial\Psi}{\partial z}=\frac{1}{2\sqrt{z}}(\eta F'-F), \tag{47}$$

$$Y=Y(\eta), \quad \varrho=\varrho(\eta), \tag{48}$$

where primes denote differentiation with respect to η.

Substituting expressions (43)–(48) into Eqs. (28)–(33), one obtains the following set of ordinary differential equations at the lowest order in $\sqrt{z}$:

$$(\varrho Y')'+\mathrm{Sc}\frac{F}{2}Y'=0, \tag{49}$$

$$V''+\frac{F}{2}V'=0, \tag{50}$$

$$\left(\frac{F'}{\varrho}\right)''+\frac{F}{2}\left(\frac{F'}{\varrho}\right)'=0, \tag{51}$$

$$\frac{1}{\mathrm{Pr}}\Theta_1''+\frac{(\gamma-1)}{2\varrho}\mathrm{Ma}^2(F'P_1-FP_1')+\frac{1}{2}(F\Theta_1'-F'\Theta_1)=0, \tag{52}$$

$$P_1'=\varrho V^2, \tag{53}$$

together with

$$\varrho=\frac{1}{Y+\epsilon(1-Y)}. \tag{54}$$

These equations are to be solved with the boundary conditions

$$\eta\to\infty: \quad Y\to 0, \quad V\to 0, \quad F'/\varrho\to W_O, \quad \Theta_1\to 0, \quad P_1\to 0, \tag{55}$$

$$\eta\to-\infty: \quad Y\to 1, \quad V\to S, \quad F'/\varrho\to 1, \quad F\to\eta, \quad \Theta_1'\to 0. \tag{56}$$

Note that at this lowest order one can only match the swirl intensity at $r\to 1^-$, i.e., $V=S$. To match exactly the specific solid body rotation $V=Sr$, or any other tangential velocity distribution of the emerging swirling jet, would require the next order of the expansion in powers of $\sqrt{z}$ of the self-similar solution. The same can be said of the pressure because no boundary condition for P_1 can be specified as $\eta\to-\infty$. However, as we shall see, this lowest order self-similar solution provides a very good approximation for small z if one uses it as part of a composite solution that takes into account the inlet boundary conditions, and it suffices for our main objective here of providing an alternative with continuous radial derivatives to initial conditions (35)–(42) to start the numerical integration of Eqs. (28)–(33). The second order correction to the self-similar solution may be obtained in an analogous way to that described in Ref. 4 for the incompressible, single-species flow, but now, in a compressible, two-species flow, the resulting ordinary differential equations are much more involved.

To solve numerically the above equations we use the subroutine BVP4C of MATLAB, which implements a collocation method for solving a system of ordinary differential equations with two-point boundary conditions, starting from an initial guess. The boundary conditions (55) and (56) are imposed at $\eta_{\max}$ and $\eta_{\min}$, respectively, whose absolute values are chosen large enough for the solution to be independent of them. As the initial guess we use tanh-like functions

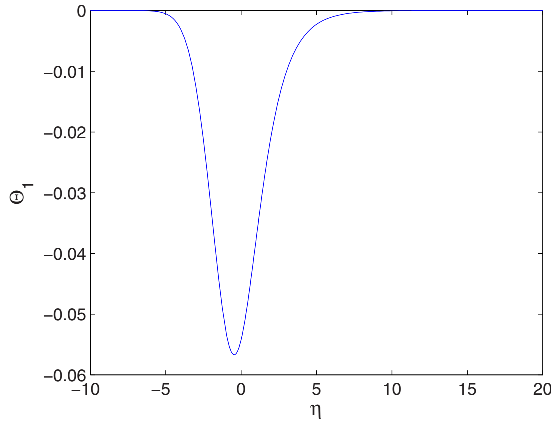

FIG. 4. (Color online) Temperature correction Θ_1 as function of η for Ma=0.5, Pr=0.7, γ=1.4, and the same remaining parameters used in Fig. 3.

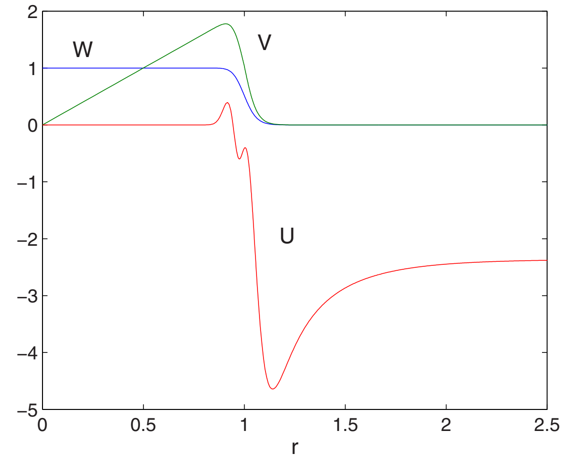

FIG. 5. (Color online) Radial profiles of the velocity components at z=0.001, and the same parameters of Figs. 2–4.

for Y, F'/ϱ, and V, and constant functions for P_1 and Θ_1. Equations (49) and (51), together with Eq. (54), for F and Y (i.e., the solutions for W, U, Y, and ϱ), are decoupled from the solutions for V, P_1, and Θ_1, depending only on the parameters W_O, Sc, and ϵ. As mentioned above, this self-similar solution for an incompressible flow without swirl was found by Sánchez-Sanz *et al.*[24] Figure 2 depicts $W=F'/\varrho$ and Y as functions of η for a hydrogen-air mixture (Sc=1.39, ϵ=0.07) in the absence of coflow (W_O=0).

The tangential velocity V [Eq. (50)] depends also on the swirl parameter S through the boundary condition as $\eta \to -\infty$, and so does the pressure correction P_1 [Eq. (53)]. In fact, it is easy to see from the equations and boundary conditions that $V=SF'/\varrho$. Figure 3 displays these functions for S=2, and the same parameters used in Fig. 2. Finally, the temperature correction Θ_1 depends additionally on the Mach number Ma, the Prandtl number Pr, and γ [Eq. (52)]. This temperature correction is depicted in Fig. 4 for Ma=0.5, Pr=0.7, and γ=1.4 (in addition to the same values used in Fig. 3 for the remaining parameters). It is interesting to note that at this lowest order in $\sqrt{z}$ of the self-similar solution, compressibility effects are only visible in the temperature distribution because the density is independent of Ma and because of the use of the variable $\bar{P}$ for the pressure. Rotation then affects the pressure distribution just through the swirl number S, which affects the temperature distribution only if Ma$\neq 0$.

Once the similarity solution is found at its lower order, the radial profiles of the mass fraction, density, velocity, pressure, and temperature at a fixed value of $z \ll 1$ are given by the following composite solutions:

$$Y(r) = Y(\eta), \quad \varrho(r) = 1/[Y + \epsilon(1 - Y)], \tag{57}$$

$$W(r) = \frac{F'(\eta)}{\varrho}, \quad U(r) = \frac{1}{2\varrho\sqrt{z}}[\eta F'(\eta) - F(\eta)], \tag{58}$$

$$V(r) = \begin{cases} S(r-1) + V(\eta) & \text{for } 0 \le r \le 1 \\ V(\eta) & \text{for } r > 1, \end{cases} \tag{59}$$

$$\bar{P}(r) = \begin{cases} \dfrac{1}{\gamma\,\mathrm{Ma}^2}[e^{[(S^2\gamma\,\mathrm{Ma}^2)/2](r^2-1)} - 1] + \sqrt{z}P_1(\eta) & \text{for } 0 \le r \le 1 \\ \sqrt{z}P_1(\eta) & \text{for } r > 1, \end{cases} \tag{60}$$

$$\Theta(r) = 1 + \sqrt{z}\Theta_1(\eta), \tag{61}$$

with $r=1+\sqrt{z}\eta$. For Ma=0 (incompressible flow), Eq. (60) has to be substituted by

$$\bar{P}(r) = \begin{cases} \dfrac{S^2}{2}(r^2 - 1) + \sqrt{z}P_1(\eta) & \text{for } 0 \le r \le 1 \\ \sqrt{z}P_1(\eta) & \text{for } r > 1. \end{cases} \tag{62}$$

Figures 5–7 show these profiles for z=0.001 and the same set of parameters used in Figs. 2–4, except for Θ (Fig. 7) that is plotted for different values of Ma. It is observed in these figures that the radial velocity U shows a double-hump structure in the mixing-layer region, where it first increases from its zero value inside the jet, then decreases abruptly, but with a hump in between, and finally increases to reach an asymptote as $r \to \infty$ corresponding to the jet entrainment rate at the given axial location z, $(-\varrho U)_{r\to\infty}=F_\infty/(2\sqrt{z})$ (with $F_\infty \simeq 2.1461$ in the case plotted). On the other hand, Fig. 6 shows that the radial profile of the mass fraction Y (and, consequently, of the density ϱ) decreases (increases) more

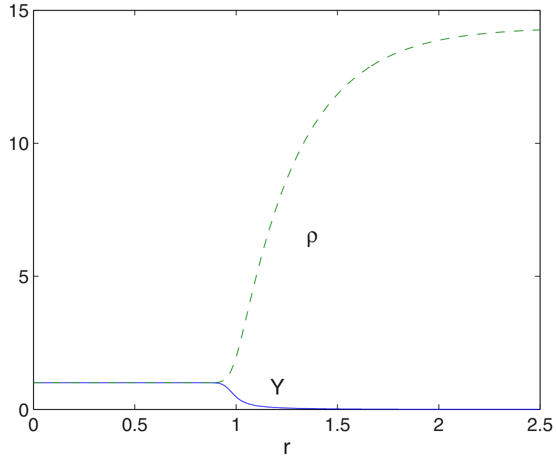

FIG. 6. (Color online) Radial profiles of the mass fraction and density at $z=0.001$, and the same parameters of Figs. 2–4.

slowly toward zero (toward ϵ^{-1}) as $r\to\infty$ than the axial and azimuthal velocity components. This behavior is due to the small value of ϵ so that the light gas jet expands quickly by diffusion into the heavier ambient gas just as the jet emerges from $z=0$ (see also Fig. 2). Finally, it is clear in Fig. 7 that the thermal (cooling) effect associated to the expansion of the light gas jet increases with the Mach number. However even for Ma of order unity this initial cooling of the emerging jet is small.

IV. RESULTS AND DISCUSSION

A. Numerical method and validation with theoretical results

To solve numerically Eqs. (27)–(33) we use second order finite differences in the axial direction and a pseudospectral, Chebyshev collocation method in the radial direction. The boundary condition (26) at infinity is applied at a truncated radial distance $r_{\max}$, chosen large enough to ensure that the results do not depend on that truncated distance. To map the interval $0\leq r\leq r_{\max}$ into the Chebyshev polynomial domain $-1\leq s\leq 1$, we use the transformation

$$r=c_1\frac{1+s}{c_2-s},\quad \text{with } c_2=1+\frac{2c_1}{r_{\max}}. \tag{63}$$

The Chebyshev variable s is discretized in the Gauss–Lobatto points $s_i=\cos(\pi i/N)$, $i=0,\ldots,N$,[26] so that approximately half of the resulting nodes r_i are concentrated in the interval $0\leq r\leq c_1$.[27] This transformation allows large values of r to be taken into account with relatively few Chebyshev basis functions. In the computations reported below, we have used values of c_1 between 1 and 5, $r_{\max}$ between 50 and 300, and N between 100 and 600.

Once the parabolic equations (27)–(33) are discretized radially, they are solved in the streamwise direction z by "marching" with a second order, backward finite differences technique in which the diffusive terms are discretized using a Crank–Nicolson method. At each $z_j=j\Delta z$ station, where Δz is the axial step size, the nonlinear equations are solved iteratively with the following scheme: First we solve the transport equations (28) and (31)–(33) for ϕ_i^j, $i=0,\ldots,N$ (the superscript is for the axial location, the subscript for the radial node, and $\phi=Y$, V, W or Θ) using the previously found values of ϕ_i^{j-1} and ϕ_i^{j-2} in the second order backward differences, and approximating initially ϕ_i^j in the nonlinear terms by their values at the previous station z_{j-1}; then, Eqs. (30), (29), and (27) are used to compute $\bar{P}$, ρ, and U, respectively, at z_j, using the previously obtained approximations of the remaining variables at z_j; the process is repeated, replacing the computed approximations for the flow variables at z_j in the nonlinear terms, until convergence is reached within a given tolerance. Usually, between 5 and 15 iterations are sufficient to reach convergence with a tolerance of the order of $(\Delta z)^2$. This marching process is started at $z=z_2$ using the self-similar solution of the preceding section at $z=z_1=\Delta z$, and boundary conditions (35)–(40) at $z=z_0=0$. Actually, in order to improve the accuracy of the starting solution at $z=z_1=\Delta z$, and therefore to reduce the number of iterations for $z\geq z_2$, the self-similar solution is corrected at $z=z_1$ through a few iterations with the above scheme, but using first order finite differences for the axial derivatives.

To check the accuracy of the numerical technique, and to find the optimal numerical parameters Δz, N, c_1, and $r_{\max}$, we

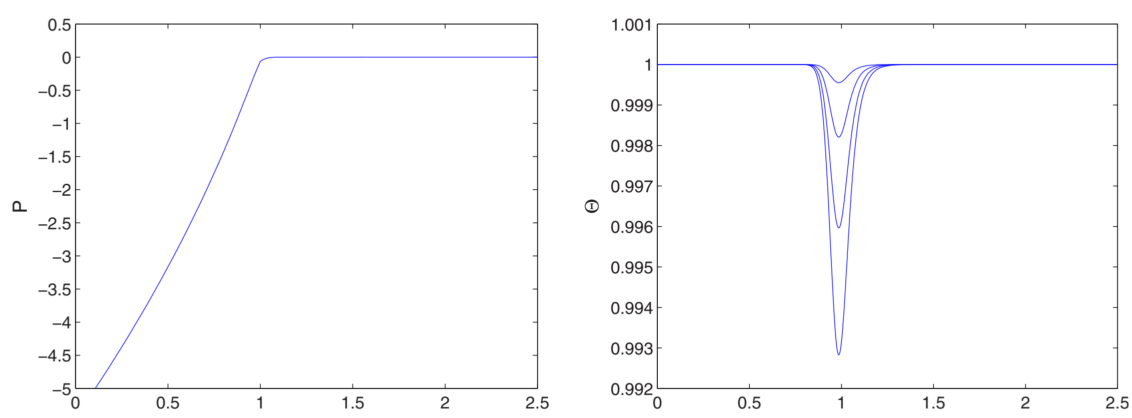

FIG. 7. (Color online) Radial profile of the pressure (left) and temperature (right) at $z=0.001$ for the same parameters of Figs. 2–4, but for Ma $=0.25,0.5,0.75,1$ (from top to bottom) in the temperature.

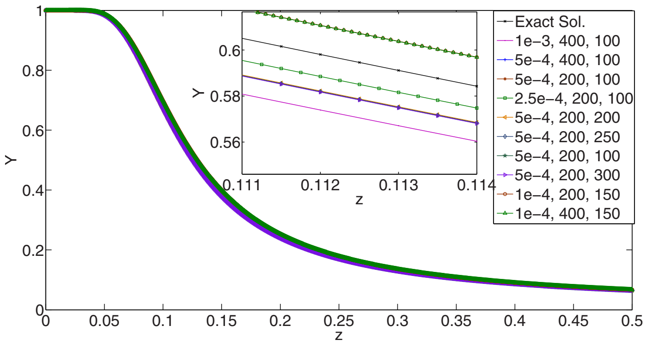

FIG. 8. (Color online) Comparison between the exact solution at the axis for Y [Eq. (65)] and the numerical solutions obtained with different values of Δz, N, and $r_{\max}$, as indicated in that order in the legend ($c_1=2$ in all cases). $\mathrm{Sc}=1.39$ and $\epsilon=0.07$.

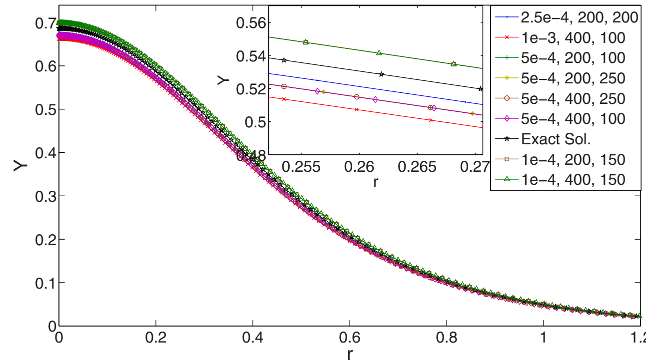

FIG. 9. (Color online) Numerical radial profiles of Y at $z=0.1$ compared to the exact solution (64) for the same cases of Fig. 8.

have made several convergence studies for simplified cases where either an analytical exact solution or an analytical asymptotic solution exists. The first case corresponds to a swirl-free jet ($S=0$ so that $V=0$) with a coflow $W_O=1$. In the absence of swirl there is no radial pressure variation so that the flow will remain isobaric and isothermal, $\bar{P}=0$ and $\Theta=1$ everywhere, and Eq. (29) reduces to $\varrho=1/[Y+\epsilon(1-Y)]$. In addition, a coflow $W_O=1$ implies that $W=1$ everywhere, simplifying the mathematical problem to a great extent. In fact, an analytical solution for Eqs. (27) and (28) in this case was found by Sánchez *et al.*,[28] which for ϱ and Y can be written as

$$\frac{1-\epsilon\varrho}{1-\epsilon}=\frac{Y}{Y(1-\epsilon)+\epsilon}=\frac{\mathrm{Sc}}{2z}e^{-\mathrm{Sc}\,r^2/4z}\int_0^1 s e^{-\mathrm{Sc}\,s^2/4z} I_0\left(\frac{\mathrm{Sc}\,rs}{sz}\right)ds, \qquad (64)$$

where I_0 is the modified Bessel function of order zero.[29] Along the axis ($r=0$), this solution simplifies to

$$\frac{1-\epsilon\varrho}{1-\epsilon}=\frac{Y}{Y(1-\epsilon)+\epsilon}=1-e^{-\mathrm{Sc}/4z} \quad \text{for} \quad r=0. \qquad (65)$$

Figures 8 and 9 compare these analytical solutions to the numerical ones for a hydrogen-air mixture ($\mathrm{Sc}=1.39$ and $\epsilon=0.07$). It is observed that the agreement is very good at every axial distance z when $\Delta z<10^{-3}$, $N>100$, and $r_{\max}>100$. Actually, the insets of these figures show that the most relevant parameter for accuracy is Δz, in such a way that for $N>100$ and $r_{\max}>100$ the convergence of the numerical solution toward the exact one improves only by diminishing the axial step size, owing to the high accuracy of the Chebyshev pseudospectral method.

The above convergence study is not enough because a coflow with $W_O=1$ smoothes out the radial profiles near the exit $z=0$, and the numerical accuracy needed to catch the jet flow is much less severe than that needed for jets without coflow. The above comparison is however interesting because it involves two species and, therefore, a distribution of mass fraction Y, and because it is made against an *exact* solution (64) of the equations. To complement this, we now compare the numerical solutions with *asymptotic* analytical solutions for a swirling jet emerging in a fluid at rest (without coflow, $W_O=0$), but corresponding to a single-species ($\epsilon=1$, and $Y=1$ everywhere). In particular, we consider the Schlichting–Görtler–Loitsianskii asymptotic solution[30,31] for the far-field decay of an incompressible ($\varrho=1$) swirling jet (see also Refs. 4 and 32). This solution, asymptotically valid for $z\gg1$, but sufficiently accurate even for $z=O(1)$, is written in terms of the self-similar variable

$$\xi=\frac{\sqrt{M}r}{z+z_0}, \qquad (66)$$

where

$$M=2\int_0^\infty [W^2+\bar{P}]r\,dr \qquad (67)$$

is the so-called flow force (or nondimensional momentum transfer, see, e.g., Ref. 33), and z_0 is the so-called virtual origin,[34] as

$$W=\frac{512M}{3(z+z_0)}\frac{1}{\left(\frac{64}{3}+\xi^2\right)^2}, \qquad (68)$$

$$V=\frac{8SMr}{(z+z_0)^3}\frac{1}{\left(\frac{64}{3}+\xi^2\right)^2}, \quad \bar{P}=-\frac{32S^2M}{3(z+z_0)^4}\frac{1}{\left(\frac{64}{3}+\xi^2\right)^3}. \qquad (69)$$

The flow force M and the virtual origin z_0 are functions of the swirl parameter S. For a uniform axial flow at the inlet with the jet rotating as a rigid body, Eq. (67) yields $M=1-S^2/4$. However, $z_0(S)$ has to be determined numerically by solving the jet developing region, for which the asymptotic solution is not valid. For this reason, we will compare our numerical solution for $\epsilon=1$ and $W_O=0$ with the self-similar solutions (68) and (69) adjusting the parameter $z_0(S)$ in the far-field. This is done in Fig. 10 for $S=0$ and in Figs. 11 and 12 for $S=0.5$. Since the flow is incompressible ($\mathrm{Ma}^2=0$), $\Theta=1$ everywhere from Eq. (33) and the boundary condition at $z=0$ so that $\varrho=1$ from the equation of state (29). In the boundary condition (38) at $z=0$ we set $Y=1$ for all r so that Y will remain unity everywhere.

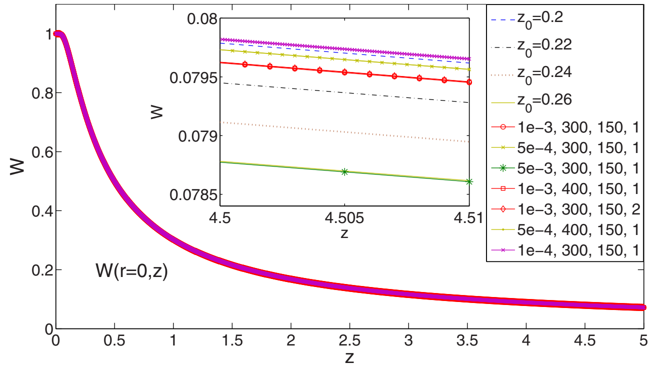

FIG. 10. (Color online) Comparison between Schlichting's asymptotic solution (68) at the axis ($r=\xi=0$) for several values of z_0 and the numerical solutions obtained with different values of Δz, N, $r_{\max}$, and c_1, as indicated in that order in the legend. $S=0$, $W_O=0$, and $\epsilon=1$ (Ma=0).

It is observed in Fig. 10 that the convergence to Schlichting's asymptotic solution (68) for $S=0$ is quite good at $z=5$, with the computed value $z_0(S=0)\simeq 0.20$ (marked with dashed lines in the figures) in close agreement with that obtained by Revuelta *et al.*[4] The main parameter for the convergence of the numerical solution is again the axial step Δz, provided that N and $r_{\max}$ are large enough and that c_1 is not too small. These figures show that for swirless jets ($S=0$), convenient choices of parameters are $\Delta z=5\times 10^{-4}$, $N=300$, $r_{\max}=150$, and c_1 between 1 and 2.

Figures 11 and 12 show that the convergence to the Schlichting–Görtler–Loitsianskii asymptotic solutions (68)

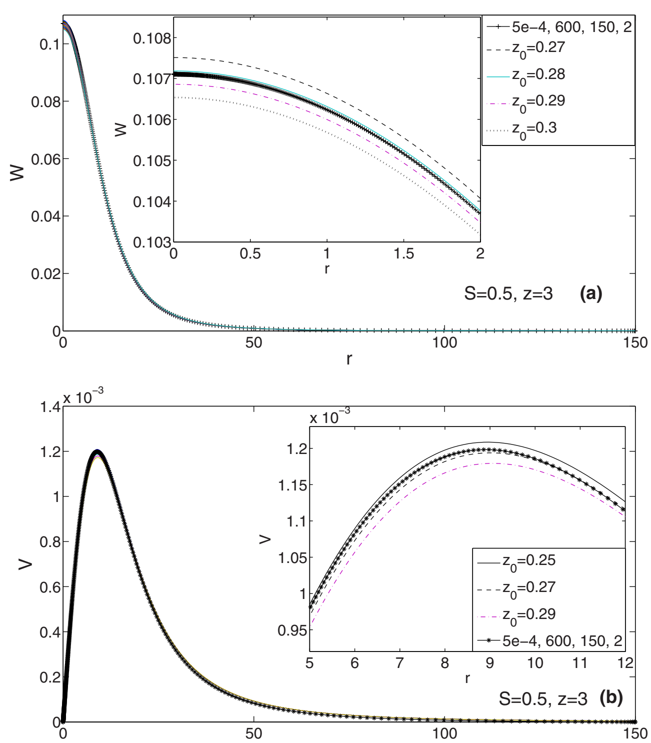

FIG. 11. (Color online) Comparison between Schlichting–Görtler–Loitsianskii asymptotic solutions (68) and (69) for $S=0.5$ and several values of z_0 (as indicated in the legend) and the numerical solution at $z=3$ obtained with $\Delta z=5\times 10^{-4}$, $N=600$, $r_{\max}=150$, and $c_1=2$. (a) Axial velocity W. (b) Azimuthal velocity V. $W_O=0$ and $\epsilon=1$ (Ma=0).

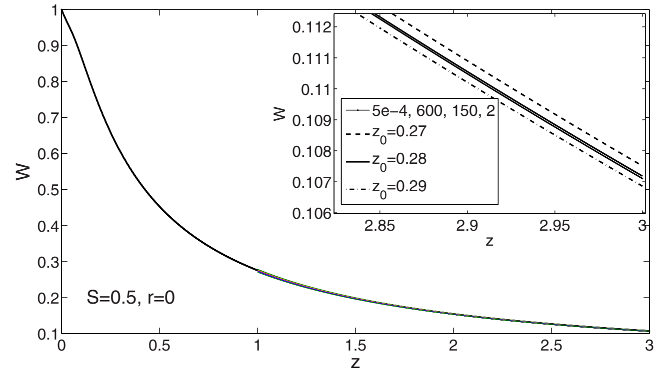

FIG. 12. (Color online) As in Fig. 11, but for the axial velocity at the axis $W(0,z)$.

and (69) is also quite good for $S=0.5$ when $z=3$. As in the case with $S=0$, the most critical numerical parameter is Δz, but now, when swirl is present in the jet flow, the required number of radial nodes N and the value of c_1 depend on the intensity of the swirl, both increasing with S. For $S=0.5$, convenient choices of the numerical parameters are $\Delta z=5\times 10^{-4}$, $N=600$, $r_{\max}=150$, and $c_1=2$ (which are the ones shown in the figures). From these figures, the computed value of $z_0(S=0.5)$ lies between 0.27 (marked with a dashed line in Figs. 11 and 12) and 0.28, in agreement with Revuelta *et al.*[4] (note that our swirl parameter S is twice the S defined by these authors so that it corresponds to their $S=0.25$).

B. Results for a homogeneous incompressible jet ($\epsilon=1$, Ma=0)

We consider first the structure of a homogeneous (single-species) jet ($\epsilon=1$) in the incompressible limit (Ma=0), i.e., the case considered in the above comparison with the asymptotic solution, but now we search systematically for changes in flow structure as both the swirl parameter S and the coflow ratio W_O are varied. In particular, we are mainly interested in the variation of the critical swirl for vortex breakdown as W_O is increased. The results in this case will serve as a reference against which to analyze the effects on the VB onset of both compressibility (Ma$\neq 0$) and the different molecular masses of the light gas jet ($\epsilon \ll 1$) that will be considered in the subsequent sections, and constitute the main objectives of the present work. In addition, the results for this case will be given here with more detail in order to describe the procedure that we use in the present work for determining the critical swirl number for VB onset with the present QC approximation. Except otherwise specified, the numerical parameters of the results reported below are $\Delta z=10^{-4}$, $N=300$, $r_{\max}=150$, and $c_1=2$, in accordance with the convergence analysis of the preceding section, with z varying between 0 and 3.

Figures 13–15 show the results for $W_O=0.05$. In particular, Fig. 13 shows the radial profiles of the axial velocity for $S=0$, $S=0.9$, $S=S_c(\epsilon=1,\ \mathrm{Ma}=0,\ W_O=0.05)\simeq 1.2220$, and $S=1.2221$. S_c is the critical swirl number for VB onset, which corresponds to the largest value of S (for given ϵ, Ma, and W_O) for which the governing parabolic equations do not break down and can be integrated numerically up to the

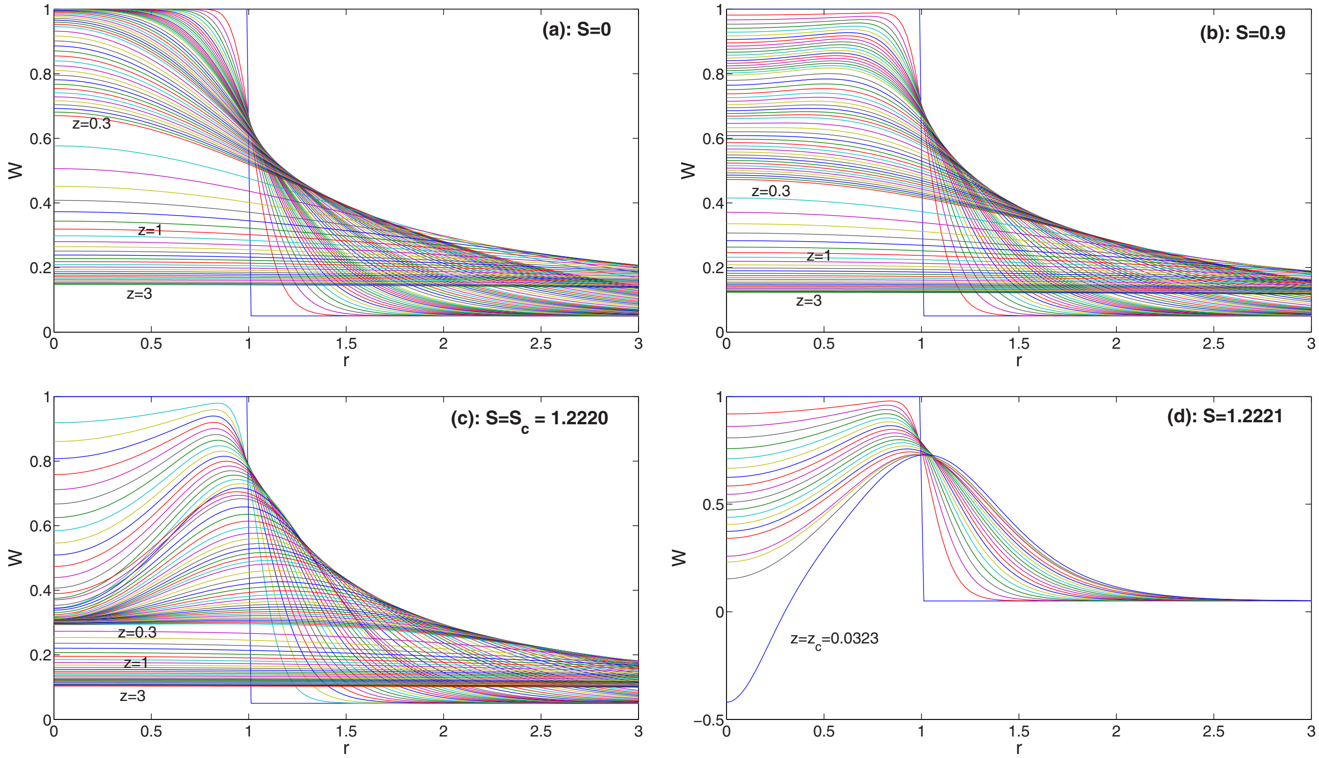

FIG. 13. (Color online) Axial velocity profiles at different values of z for $\epsilon=1$, Ma=0, $W_O=0.05$, and (a) $S=0$, (b) $S=0.9$, (c) $S=S_c=1.2220$, and (d) $S=1.2221$. In (a)–(c) the different lines correspond to values of z increasing by 0.002 between $z=0$ and 0.04, then by 0.005–0.1, by 0.01–0.3, and by 0.1 to $z=3$. In (d) the increment in z is 0.002.

maximum axial distance considered. For the next value, $S=1.2221$ (within the accuracy used here we only consider four decimal figures), the axial velocity becomes negative at the axis at $z=z_c \simeq 0.0326$, and, after that axial location, the parabolic equations cease to be valid. This is better appreciated in Fig. 14, where the evolution along z of the axial velocity at the axis, $W(0,z)$, and the pressure at the axis, $\bar{P}(0,z)$, are plotted for different values of S (for $S=0$, $\bar{P}=0$ everywhere, and it is substituted by the case $S=0.1$). For $S=1.2221$ (dashed lines) the axial velocity drops abruptly to zero at $z=z_c$, and the pressure blows up. For $S=S_c \simeq 1.2220$, the axial velocity at the axis decreases, and then increases abruptly near $z=z_c$ [see inset in Fig. 14(a)], but decays smoothly downstream as in the cases with $S<S_c$. The pressure at the axis has an analogous behavior. Therefore $S=S_c$ marks the onset of VB, with the subsequent failure of the QC approximation for $S>S_c$.[4,15–18]

To complete the picture for $W_O=0.05$, Fig. 15 shows the radial profiles of the azimuthal velocity for the same parameters as in Fig. 13 (except for the case $S=0$ that is substituted by $S=0.1$). It is observed that the swirl decays very fast, with the peak azimuthal velocity less than half the initial one already at $z=0.1$. This fast decay is much more dramatic for S close to S_c, especially just after vortex breakdown [see Fig. 15(d), where the azimuthal velocity near the axis becomes very small as z approaches z_c].

Similar trends are observed for increasing values of W_O. Figures 16–18 show the axial evolution of the axial velocity

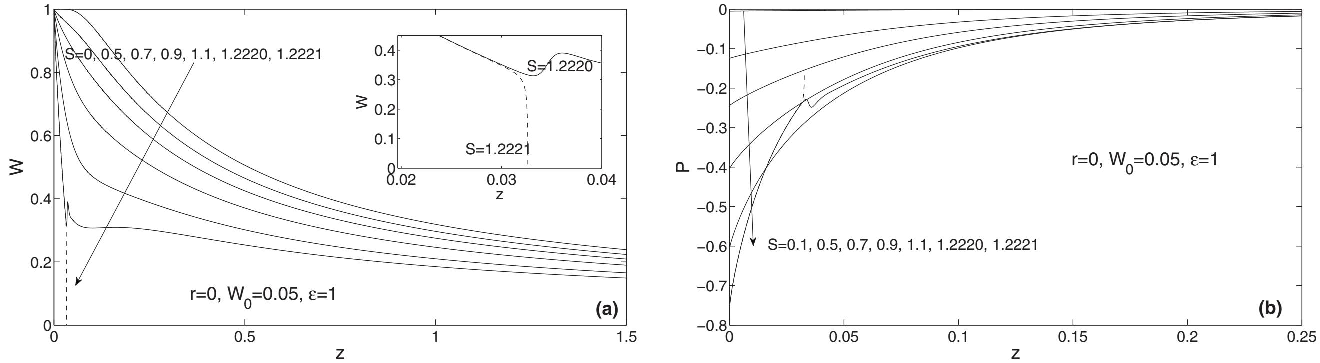

FIG. 14. (a) Axial evolution of the axial velocity at the axis for different values of S, as indicated. (b) The same for the pressure $\bar{P}$ at the axis. $\epsilon=1$, Ma=0, and $W_O=0.05$.

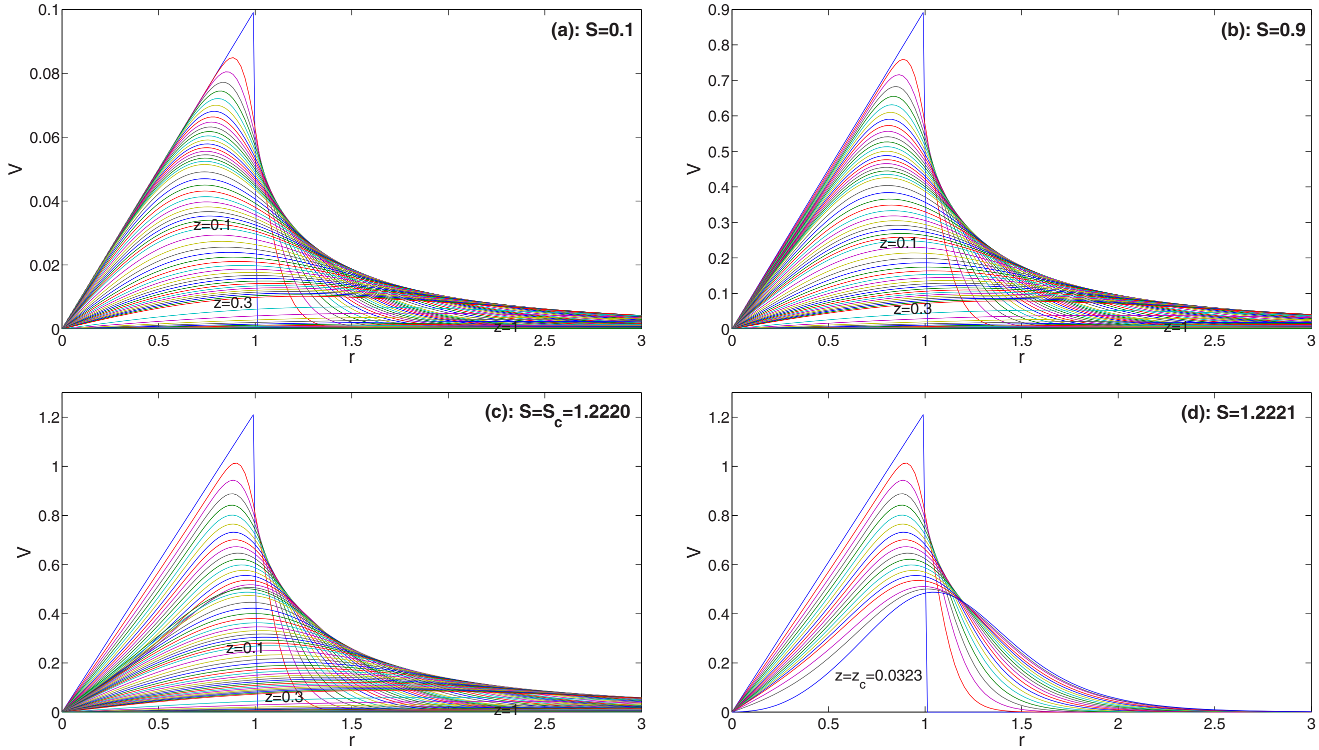

FIG. 15. (Color online) As in Fig. 13, but for the azimuthal velocity, and for $S=0.1$ in (a) instead of $S=0$.

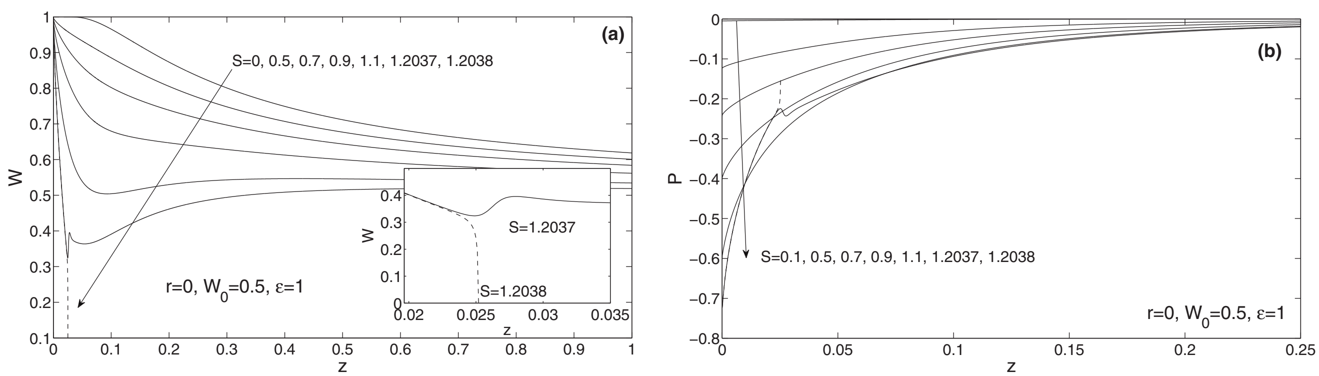

FIG. 16. As in Fig. 14, but for $W_O=0.5$.

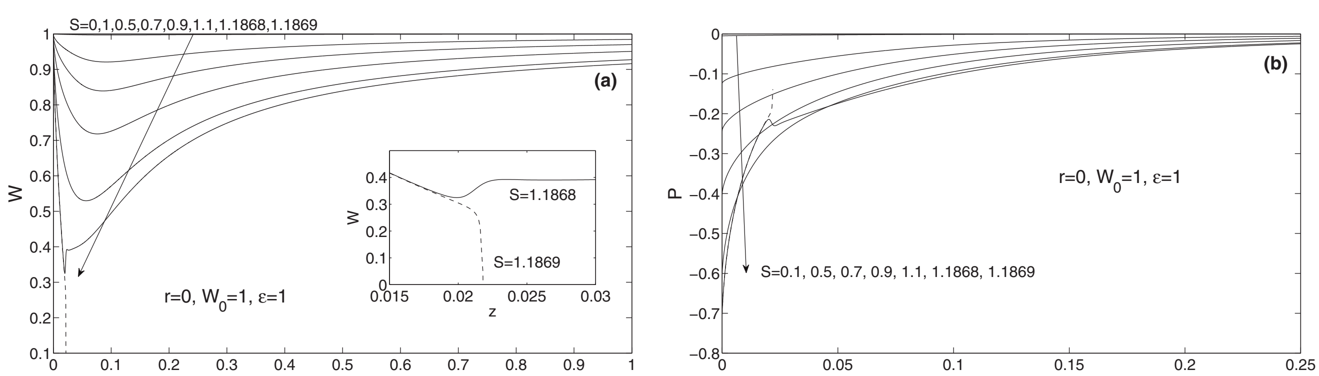

FIG. 17. As in Fig. 14, but for $W_O=1$.

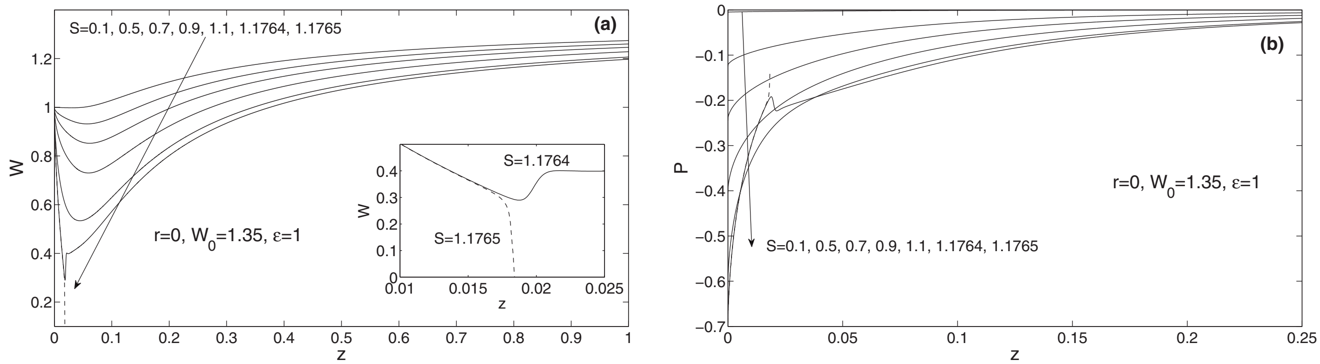

FIG. 18. As in Fig. 14, but for $W_O=1.35$.

and the pressure at the axis for $W_O=0.5$, 1 and 1.35 (the numerical parameters used in the computations are the same given above for $W_O=0.05$). In all these cases, the axial velocity at the axis becomes smaller than W_O in some axial region as S approaches S_c, and the critical swirl S_c decreases as the coflow W_O increases. This behavior is better appreciated in Fig. 19, which shows the radial profiles of the axial velocity at different z for $S=S_c(W_O)$, $W_O=0.5$, 1 and 1.35 [compare with Fig. 13(c)], with the computed function $S_c(W_O)$ plotted in Fig. 20.

As the swirl approaches the critical level S_c, the axial pressure gradient at the axis increases abruptly, causing a rapid decay of the axial velocity at the axis near the flow exit $z=0$. For $S>S_c$, the axial velocity at the axis becomes negative for some $z=z_c \ll 1$ (vortex breakdown), and the present QC approximation ceases to be valid. As the coflow W_O increases, the only qualitative difference is that the axial gradient of the pressure is a bit larger near the axis for a given S close to S_c [compare the (b) parts of Figs. 14 and 16–18] due to the increasing axial momentum outside the jet. Since the momentum flux at the axis remains the same and the pressure rise at the axis becomes more abrupt for a given S as W_O increases, vortex breakdown is reached for a smaller value of the swirl, and S_c decreases slightly as W_O increases. This is shown in Fig. 20, where the function $S_c(W_O)$ is plotted for all the values of W_O considered.

C. Results for a hydrogen-air incompressible jet ($\epsilon=0.07$, Ma=0)

We first show in this case the results for the structure with coflow $W_O=0.05$, i.e., practically without coflow, and compare them with the results for $\epsilon=1$ reported above. Figure 21 shows this comparison for the downstream evolutions of the axial velocity at the axis, $W(0,z)$, and the pressure at the axis, $\bar{P}(0,z)$, when the swirl number S is increased from zero to its critical value for vortex breakdown.

The main difference between the two cases is that the depression originated by the swirl is less concentrated near the axis (the axial pressure gradient is smaller) in the case of a light jet ($\epsilon=0.07$) than in the case of a homogeneous jet ($\epsilon=1$) [see Fig. 21(b)]. As a consequence, the critical swirl for vortex breakdown for $\epsilon=1$ is smaller than in the case with $\epsilon=0.07$: $S_c=1.2220$ for $\epsilon=1$, while $S_c=1.2784$ for

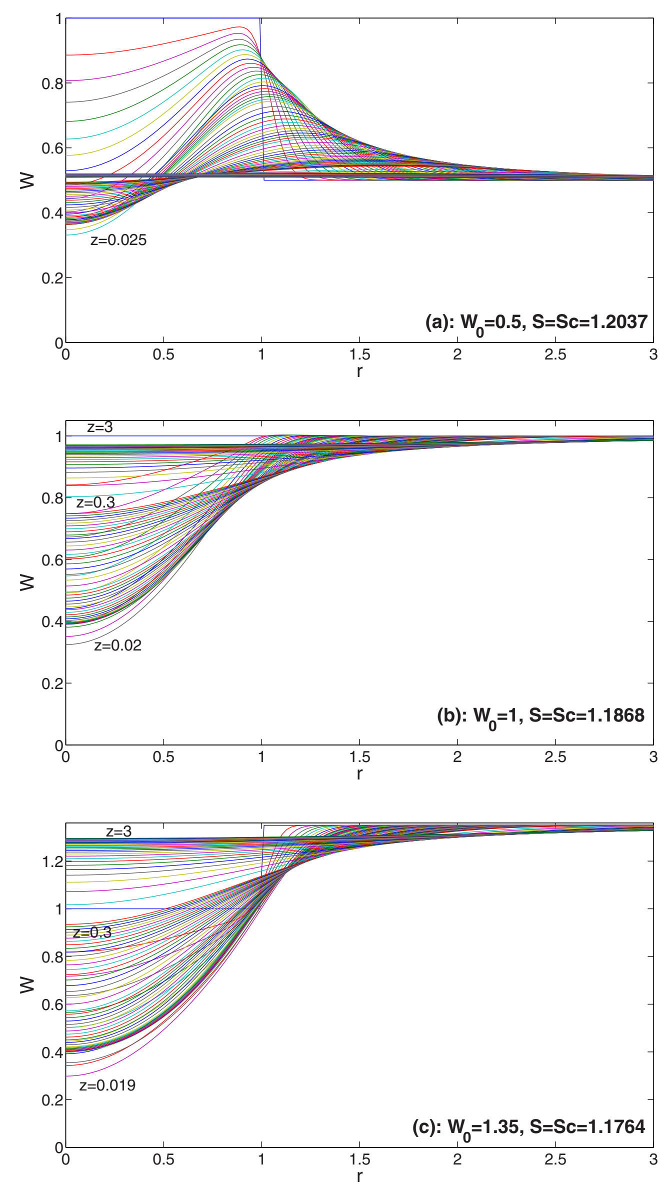

FIG. 19. (Color online) Axial velocity profiles at different z for $\epsilon=1$, Ma=0, (a) $W_O=0.5$, (b) $W_O=1$, and (c) $W_O=1.35$, for $S=S_c(W_O)$, as indicated in the legends. The different lines correspond to the same values of z shown in Fig. 13.

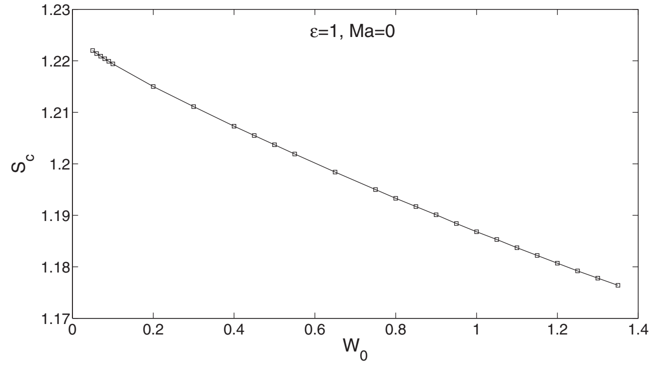

FIG. 20. S_c vs W_O for $\epsilon=1$ and Ma=0.

$\epsilon=0.07$. That is to say, the abrupt axial gradient of the pressure that precedes vortex breakdown as the swirl S increases is retarded in the case of a light jet due to the fact that the swirl is less effective in creating an axial depression when the relative mass of the jet is smaller so that one needs a larger swirl intensity to reach the appropriate pressure gradient for breakdown in the light gas jet case.

This behavior also explains the differences observed in the axial profiles of the axial velocity at the axis depicted in Fig. 21(a). Without swirl ($S=0$), the light jet is more concentrated near the axis than the homogeneous jet due to the smaller axial momentum of the light gas, which is "stopped" more quickly than the homogeneous jet by the heavier surrounding gas. However, as the swirl increases, the larger axial gradient in the pressure originated in the case of the heavier homogeneous jet changes this behavior, restraining the axial momentum of the jet which results in a larger axial gradient of the axial velocity than in the case of a light gas jet.

To see better this last mentioned behavior of the axial velocity, Fig. 22 compares the radial velocity profiles for $\epsilon=1$ and for $\epsilon=0.07$ at their respective critical swirls S_c. The light gas jet remains more concentrated near the axis [Fig. 22(b)], but the axial velocity at the axis decays more rapidly for large z in the case of a homogeneous, heavier gas jet [Fig. 22(a)].

To finish with this case with near-absence of coflow, $W_O=0.05$, Fig. 23 shows the axial variations of the mass fraction Y and the density ϱ at the axis as the swirl is increased from zero to S_c. It is noteworthy that the effect of the swirl is not very significant in the concentration nor in the mixture density, even when approaching the critical swirl, in spite of the drastic modifications in the velocity field when vortex breakdown is approached. In fact, the radial profiles of the mass fraction Y practically do not change when the swirl increases from zero to the critical swirl number S_c, and seems to indicate that diffusion does not significantly affect the vortex breakdown phenomenon. What seems to be important for the determination of the critical swirl is the relative density of the jet in relation to the background gas.

As the coflow W_O increases, the behavior of the flow changes as in the previous section, but now these changes are more significant than in the case with $\epsilon=1$, as may be observed for $W_O=0.5$ in Fig. 24, especially in part (b) of this figure. Note that the axial gradient of the pressure increases drastically as S increases, becoming much larger than in the case with $\epsilon=1$ for the same coflow W_O. As a consequence, the critical swirl for breakdown S_c decreases now for $\epsilon=0.07$ in an amount larger than in the case with $\epsilon=1$ for the same coflow. This means that the coflow is more effective favoring vortex breakdown when the density of the interior gas jet is smaller.

The same trend is observed in Fig. 25 for $W_O=1$, decreasing the critical swirl for breakdown as the coflow increases more rapidly than in the case of a homogeneous jet. In fact, the effect of the coflow for $W_O=1$ surpasses the opposite effect of the low density at the axis, and the critical swirl for breakdown is now slightly smaller for the case of a light jet ($S_c=1.1863$ for $\epsilon=0.07$) than for a homogeneous jet ($S_c=1.1869$ for $\epsilon=1$). Thus, for $W_O \gtrsim 1$, S_c is smaller in the case with $\epsilon=0.07$ than in the case with $\epsilon=1$, decreasing S_c with W_O slightly faster in the former case. Figure 26 summarizes the computed values of S_c as a function of W_O for these two values of ϵ. Note that in the range $0.8 \lesssim W_O \lesssim 1$, the critical swirl numbers for vortex breakdown for $\epsilon=0.07$ and $\epsilon=1$ are practically the same.

Finally, it is worth commenting that as in the case of a small coflow described above, the concentration of the light gas is almost independent of the swirl when the amount of coflow increases, in spite of the strong changes originated in the flow structure when S approaches S_c. This is shown in

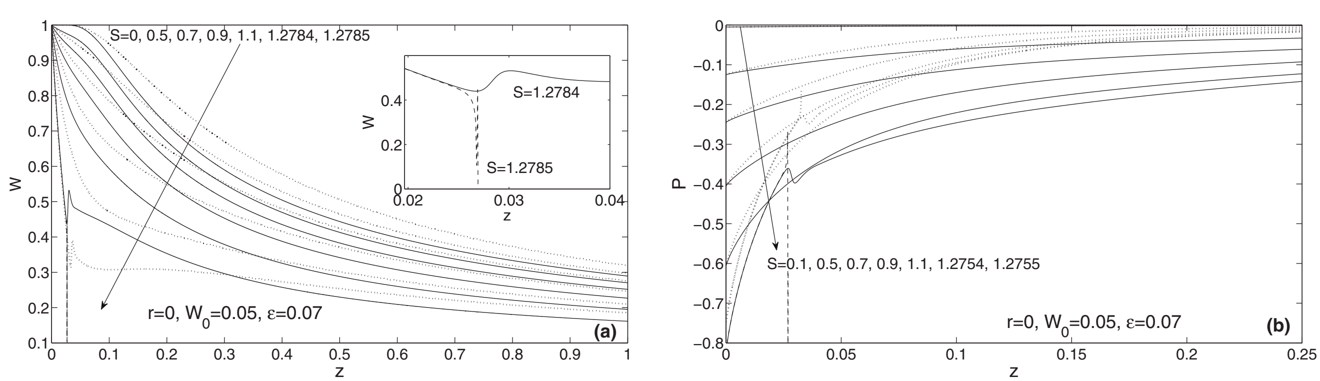

FIG. 21. Axial evolutions of the axial velocity at the axis (a), and the pressure $\bar{P}$ at axis (b), for $\epsilon=0.07$, Ma=0, $W_O=0.05$, and different values of S, as indicated. The dotted lines correspond to the results for $\epsilon=1$ (Fig. 14).

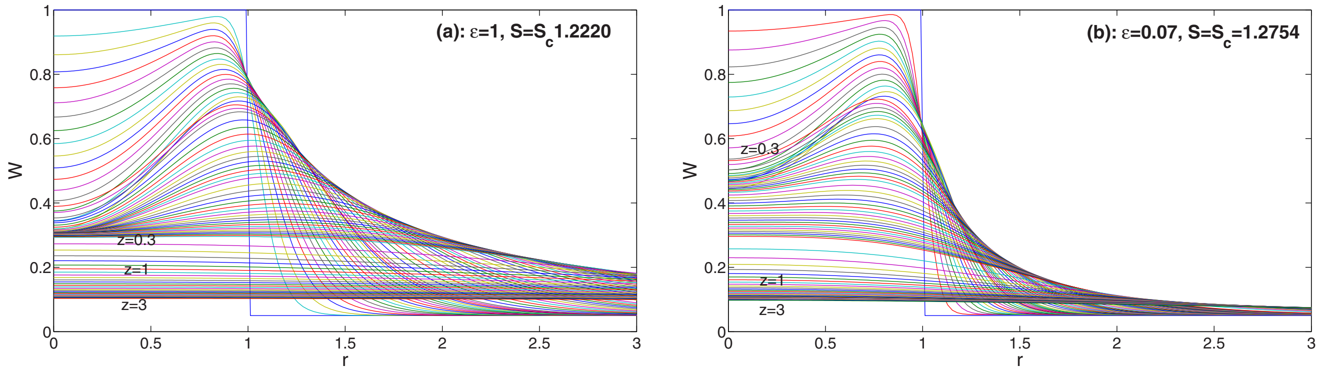

FIG. 22. (Color online) Comparison of the radial profiles of the axial velocity component at $S=S_c$ for $W_O=0.05$ when (a) $\epsilon=1$ and (b) $\epsilon=0.07$. Ma=0 in both cases. The different lines correspond to the same values of z shown in Fig. 13.

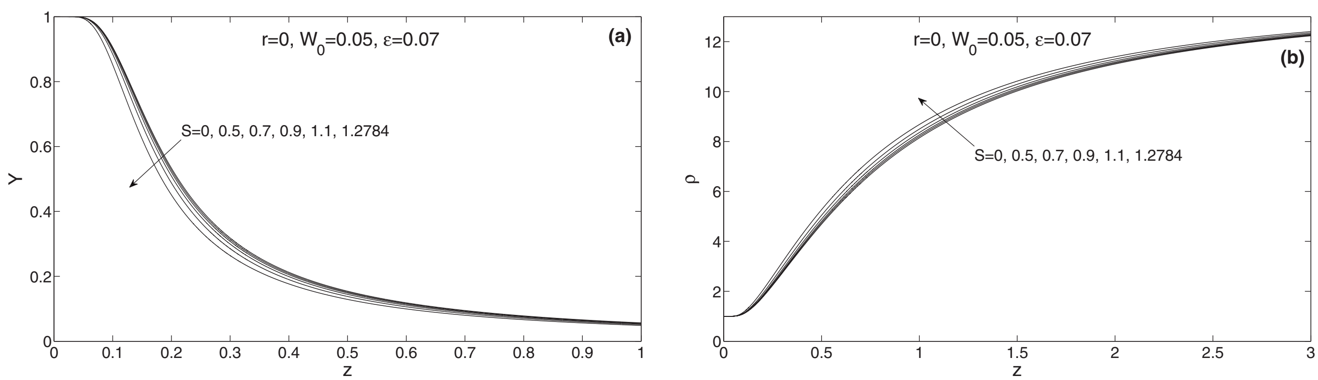

FIG. 23. (a) Axial evolutions of the H_2 mass fraction Y at the axis for different values of S, as indicated. (b) The same for the density ϱ at the axis. $\epsilon=0.07$, Ma=0, and $W_O=0.05$.

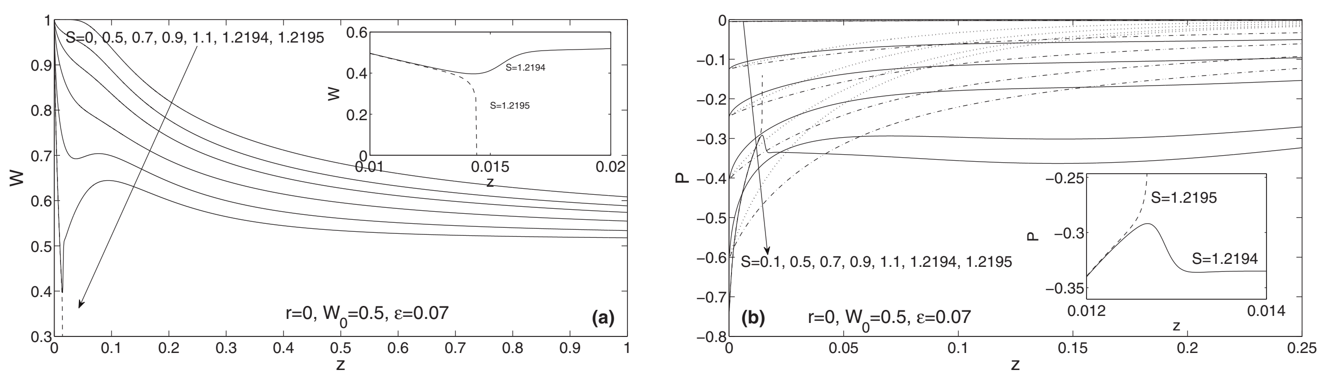

FIG. 24. As in Fig. 21 but for $W_O=0.5$. In (b) we also include the cases depicted in Fig. 21, i.e., $\epsilon=1$, $W_O=0.05$ (dotted lines), and $W_O=0.05$, $\epsilon=0.07$ (dashed-and-dotted lines).

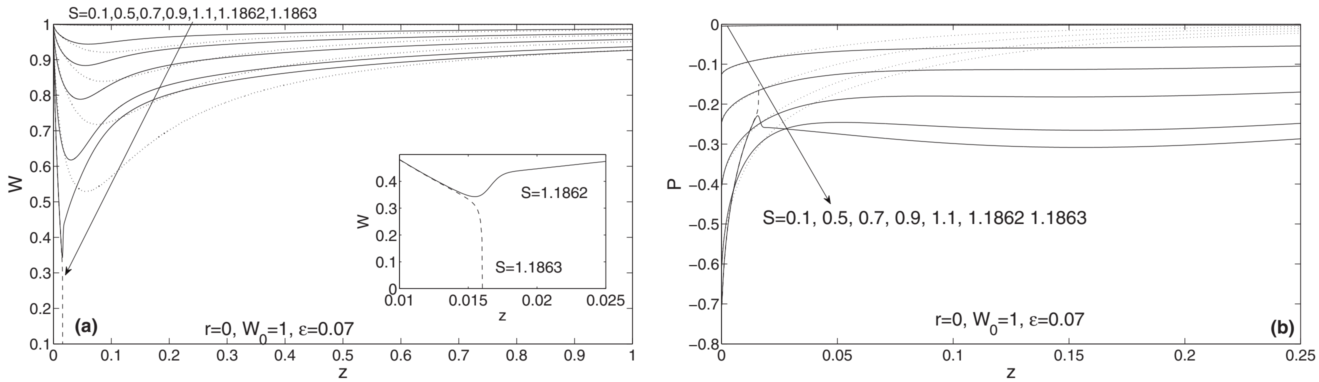

FIG. 25. As in Fig. 21 but for $W_O=1$. Dotted lines correspond to the same coflow with $\epsilon=1$.

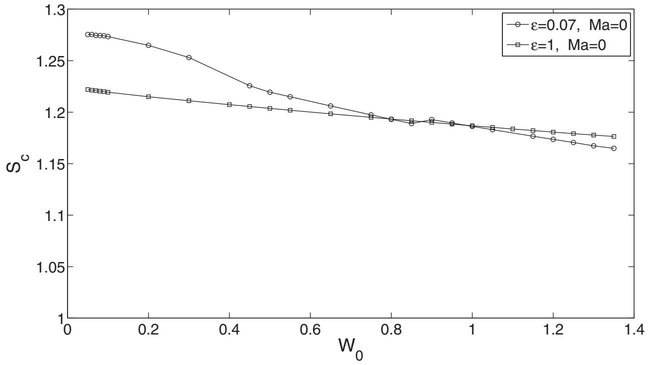

FIG. 26. S_c vs W_O for $\epsilon=0.07$ compared to the case for $\epsilon=1$.

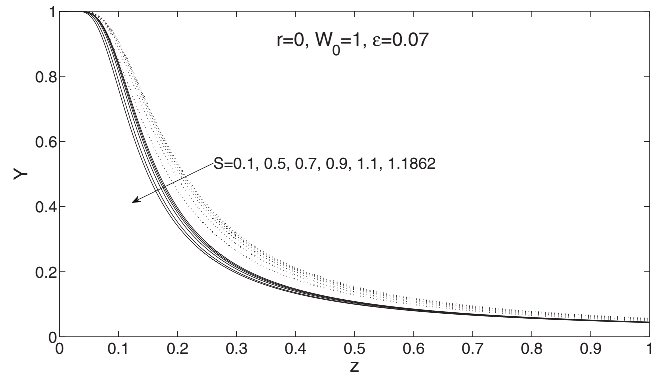

FIG. 27. As in Fig. 23(a) but for $W_O=1$ (dotted lines correspond to $W_O=0.05$).

Fig. 27 for $W_O=1$, where it is also observed that the effect of increasing the coflow W_O is to decrease slightly the diffusion of the light gas into the heavier ambient.

D. Results for a hydrogen-air ($\epsilon=0.07$) compressible jet with Ma=0.5

When compressibility effects are taken into account (Ma>0), the temperature is no longer constant ($\Theta \neq 1$) because pressure gradients may now create temperature variations [see Eq. (33)]. Since the swirl generates a depression at the axis in the flow, it affects the temperature, and therefore the density through the equation of state, which in turn modifies again the pressure distribution and the velocity field near the axis, so that the critical swirl for breakdown may change appreciably due to compressibility effects.

To try to understand these mechanisms, we consider here the case of $\epsilon=0.07$ with Ma=0.5, and, first, the case with almost absence of coflow ($W_O=0.05$). Figure 28 shows the comparison between the incompressible case (Ma=0) and the compressible one with Ma=0.5 of the downstream evolutions of both the axial velocity and the pressure at the axis for different swirl numbers. It is observed that the differences are almost negligible when the swirl is small. However, as the swirl number approaches the critical value for vortex breakdown, the compressibility effects become remarkable in the sense that the axial gradients close to the jet exit $z=0$ become much larger for the case Ma=0.5 than for Ma=0. As a consequence, the depression originated by the swirl is more concentrated near the axis in the compressible case with Ma=0.5, and the flow conditions for vortex breakdown are reached with a significantly lower swirl level in this compressible case so that the critical swirl for vortex breakdown is smaller for Ma=0.5 than for Ma=0 ($S_c=1.1941$ for Ma=0.5 against $S_c=1.2784$ for Ma=0).

In other words, the abrupt axial gradient of the pressure that initiates VB as the swirl S increases is enhanced by the compressibility effects due to the fact that now the swirl is more effective in creating an axial depression when the temperature increases near the axis (see below) so that one needs a lower swirl intensity to reach the appropriate pressure gradient for breakdown in the compressible jet case. Figure 29 shows this effect in the axial velocity profiles at different values of z for $S=1.1$, which is close to S_c. The axial velocity defect near the axis is remarkably larger in the vicinity of the jet exit for Ma=0.5 than for Ma=0. This is explained by the significant increase in the temperature near the axis when the swirl increases [see Fig. 30(a)] so that according to the equation of state (29), the density ϱ falls below unity near the axis when z is small, where Y is close to unity [see Fig. 30(b)]. Then, by mass conservation [Eq. (27)], an abrupt axial gradient of the axial velocity near the axis is generated near the jet exit $z=0$, producing the axial velocity defect at the axis that precedes vortex breakdown. Without the heating effect near the axis (i.e., when Ma=0), this axial velocity defect is reached for larger values of S by means of just the depression generated by the swirl. This global behavior is in qualitative agreement with previous results on vortex breakdown for compressible vortices structurally different from the present one, where compressibility makes the vortex more susceptible to breakdown.[19,20]

This compressibility effect on the critical swirl number, discussed above for $W_O=0.05$, is almost independent on the coflow so that the curve $S_c(W_O)$ for Ma=0.5 is practically parallel, and below, the one discussed in the preceding section for Ma=0 (see Fig. 31).

E. Summary of the results for S_c

Figure 32 summarizes all the values of the critical swirl number for VB onset as a function of the coflow W_O computed for Ma=0, 0.1, and 0.5, and for $\epsilon=1$ and 0.07. The trend of $S_c(W_O)$ for Ma=0.5 and $\epsilon=1$ is analogous to that described in the preceding section for $\epsilon=0.07$. For weak compressibility effects (Ma=0.1) the results are obviously very similar to those corresponding to the incompressible case Ma=0. Note that the minimum value of W_O represented is 0.05. Numerical results for the flow structure with $W_O=0$ can be obtained, with similar computer cost than for $W_O>0$, for small values of the swirl S (see, e.g., Sec. IV A). However, as the swirl approaches its critical level S_c it is very difficult to start the numerical integration at $z=0$ for $W_O \lesssim 0.05$ (one needs values of Δz much smaller than the ones used in the above reported computations). For this reason the critical swirl numbers S_c have been computed only for $W_O \geq 0.05$. In any case, the values of S_c for $W_O=0$ can be easily extrapolated from the results given in Fig. 32.

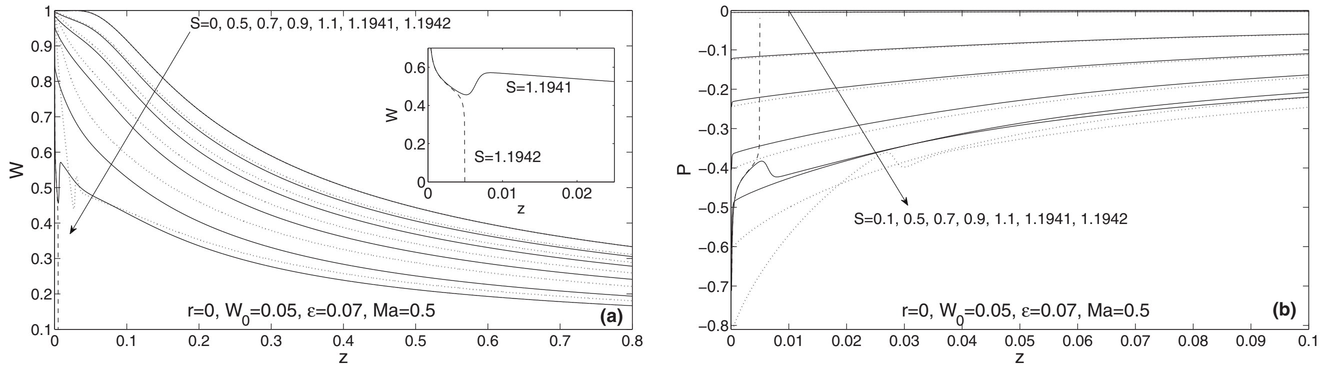

FIG. 28. Axial evolutions of the axial velocity at axis (a) and the pressure $\bar{P}$ at axis (b), for $\epsilon=0.07$, Ma=0.5, $W_O=0.05$, and different values of S, as indicated. The dotted lines correspond to the results for Ma=0 (Fig. 21).

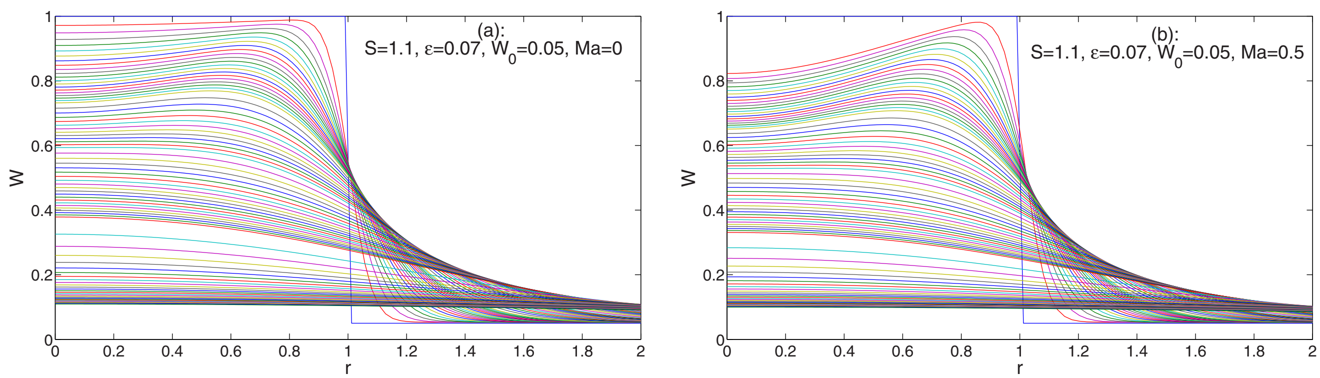

FIG. 29. (Color online) Comparison between the radial profiles of the axial velocity component for $S=1.1$, $W_O=0.05$, and $\epsilon=0.07$ when (a) Ma=0 and (b) Ma=0.5. The different lines correspond to the same values of z shown in Fig. 13.

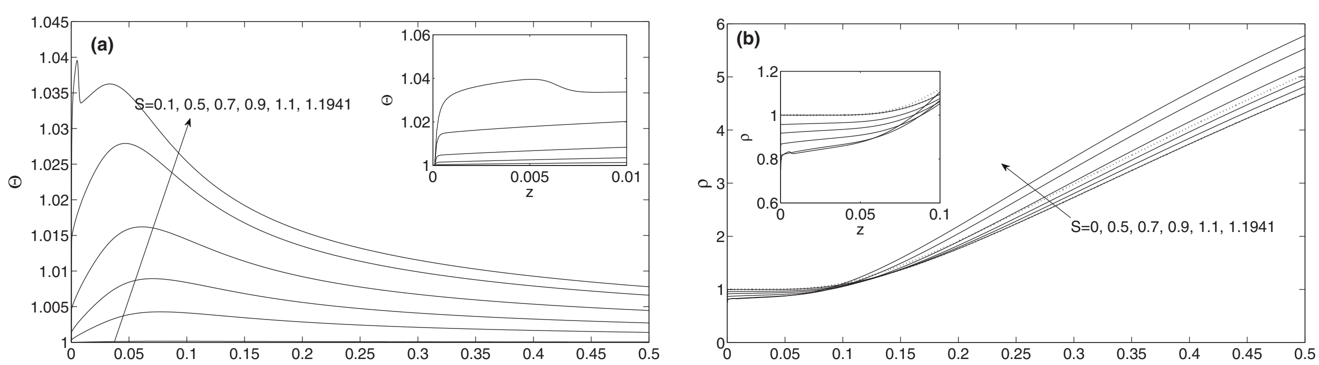

FIG. 30. Axial evolutions of the temperature Θ at axis (a) and the density ϱ at axis (b), for $\epsilon=0.07$, Ma=0.5, $W_O=0.05$, and different values of S, as indicated. The dotted lines in (b) correspond to $S=0$ and $S=0.1$ for the incompressible case (Ma=0).

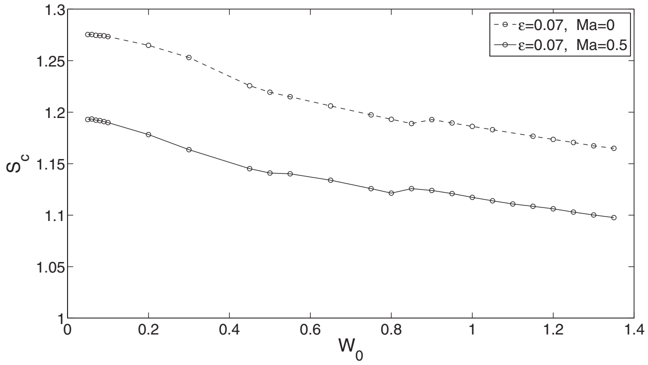

FIG. 31. S_c vs W_O for $\epsilon=0.07$ and Ma=0.5 compared to the case for Ma=0.

V. SUMMARY AND CONCLUSIONS

We have analyzed in this work the axisymmetric flow structure and the vortex breakdown onset of a swirling gas jet discharging into an ambient constituted by a gas of much larger molecular weight. The results have been compared with those corresponding to a swirling jet discharging into the same ambient gas, characterizing the effect on the vortex breakdown onset of the disparity of molecular weights between the jet and the ambient, in addition to the effects of compressibility and of the relative velocity (coflow) of the ambient gas. This problem is of particular interest in some combustion processes, where the fuel, constituted by a light gas such as H_2, is injected into an oxidant ambient (e.g., air) of much larger molecular weight, and where the vortex breakdown phenomenon of the discharging swirling jet is sought for flame stabilization, to enhance mixing and reduce pollution.

A quasicylindrical approximation of the flow equations, valid for high Reynolds numbers, has been used. To start the numerical integration of these equations we have used a general self-similar solution valid close to the jet exit, which is also obtained in the present work. The vortex breakdown onset is characterized by the failure of the quasicylindrical approximation.

We have considered the case of a molecular weight ratio between the jet and the ambient gas of $\epsilon=0.07$, corresponding to a hydrogen-air mixture, and compared the results with those for the homogeneous, single-species jet case ($\epsilon=1$).

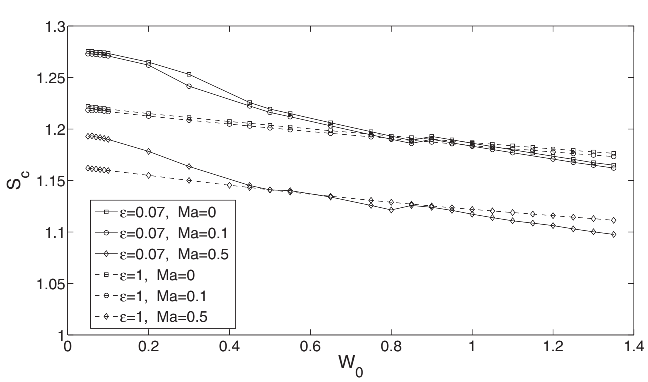

FIG. 32. S_c vs W_O for the different values of Ma and ϵ considered.

The coflow W_O has been varied from practically zero to 1.35, and the Mach number Ma from 0 to 0.5. All the results for vortex breakdown onset, i.e., for the critical swirl number for vortex breakdown, are summarized in Fig. 32. In all the cases considered the critical swirl S_c decreases as the coflow W_O increases. This is explained by the larger axial gradient of the pressure at the axis near the flow exit due to the increasing axial momentum outside the jet so that vortex breakdown is reached for a smaller value of the swirl. In the case of a light swirling jet ($\epsilon \ll 1$), the critical swirl for vortex breakdown is generally larger than in the case of a homogeneous jet ($\epsilon=1$). This is explained by the fact that the swirl is less effective in creating the abrupt axial gradient of the pressure drop near the axis that precedes vortex breakdown as the swirl S increases when the relative mass of the jet is smaller so that one needs a larger swirl intensity to reach the appropriate axial pressure gradient for breakdown in the light gas jet case. However, for $W_O \gtrsim 1$, the opposite effect of coflow dominates, and S_c becomes slightly smaller for $\epsilon \ll 1$ than for $\epsilon=1$. Finally, the effect of compressibility is always to diminish S_c due to the abrupt temperature rise near the jet exit when S is high enough, which enhances the axial pressure rise at the flow exit and makes the swirling jet more susceptible to vortex breakdown. This last result is in qualitative agreement with previous ones for compressible (shock-free) vortex breakdown in different types of vortices.[19,20]

ACKNOWLEDGMENTS

This research has been supported by the Ministerio de Educación y Ciencia of Spain under Grant No. FIS2007-60161.

[1] O. Lucca-Negro and T. O'Doherty, "Vortex breakdown: A review," Prog. Energy Combust. Sci. **27**, 431 (2001).
[2] M. R. Ruith, P. Chen, E. Meiburg, and T. Maxworhy, "Three-dimensional vortex breakdown in swirling jets and wakes: Direct numerical simulation," J. Fluid Mech. **486**, 331 (2003).
[3] A. Revuelta, "On the axisymmetric vortex breakdown of a swirling jet entering a sudden expansion pipe," Phys. Fluids **16**, 3495 (2004).
[4] A. Revuelta, A. L. Sánchez, and A. Liñán, "The quasi-cylindrical description of submerged laminar swirling jets," Phys. Fluids **16**, 848 (2004).
[5] A. Revuelta, A. L. Sánchez, and A. Liñán, "Confined swirling jets with large expansion ratios," J. Fluid Mech. **508**, 89 (2004).
[6] J. Panda and D. K. Maclaughlin, "Experiments on the instabilities of a swirling jet," Phys. Fluids **6**, 263 (1994).
[7] P. Billant, J.-M. Chomaz, and P. Huerre, "Experimental study of vortex breakdown in swirling jets," J. Fluid Mech. **376**, 183 (1998).
[8] F. Gallaire, S. Rott, and J. M. Chomaz, "Experimental study of a free and forced swirling jet," Phys. Fluids **16**, 2907 (2004).
[9] H. Z. Liang and T. Maxworthy, "An experimental investigation of swirling jets," J. Fluid Mech. **525**, 115 (2005).
[10] I. K. Toh, G. Honnery, and J. Soria, "Axial plus tangential entry swirling jets," Exp. Fluids **48**, 309 (2010).
[11] A. H. Lefebvre, *Gas Turbine Combustion*, 2nd ed. (Taylor & Francis, New York, 1999).
[12] J. Ji and J. P. Gore, "Flow structure in lean premixed swirling combustion," *Proceedings of the Combustion Institute* (Elsevier, Amsterdam, 2002), Vol. 29, pp. 861–867.
[13] Y. Huang and V. Yang, "Dynamics and stability of lean-premixed swirl-stabilized combustion," Prog. Energy Combust. Sci. **35**, 293 (2009).
[14] M. G. Hall, "The structure of concentrated vortex cores," *Progress in Aeronautical Sciences* (Pergamon, New York, 1966), Vol. 7, pp. 53–110.
[15] M. Hall, "Vortex breakdown," Annu. Rev. Fluid Mech. **4**, 195 (1972).
[16] P. Beran and F. Culik, "The role of nonuniqueness in the development of vortex breakdown in tubes," J. Fluid Mech. **242**, 491 (1992).

[17]M. A. Herrada, M. Perez-Saborid, and A. Barrero, "Vortex breakdown in compressible flows in pipes," Phys. Fluids **15**, 2208 (2003).
[18]W. Gyllenram, H. Nilsson, and L. Davidson, "On the failure of the quasi-cylindrical approximation and the connection to vortex breakdown in turbulent swirling flow," Phys. Fluids **19**, 045108 (2007).
[19]J. J. Keller, "On the practical application of vortex breakdown theory to axially axisymmetrical and three-dimensional compressible flows," Phys. Fluids **6**, 1515 (1994).
[20]K. Mahesh, "A model for the onset of breakdown in an axisymmetric compressible vortex," Phys. Fluids **8**, 3338 (1996).
[21]Z. Rusak and J. H. Lee, "The effect of compressibility on the critical swirl of vortex breakdown in a pipe," J. Fluid Mech. **461**, 301 (2002).
[22]M. Pérez-Saborid, M. A. Herrada, A. Gómez-Barea, and A. Barrero, "Downstream evolution of unconfined vortices: Mechanical and thermal aspects," J. Fluid Mech. **471**, 51 (2002).
[23]D. E. Rosner, *Transport Processes in Chemically Reacting Flow Systems* (Butterworth-Heinemann, Boston, 1986).
[24]M. Sánchez-Sanz, M. Rosales, and A. L. Sánchez, "The hydrogen laminar jet," Int. J. Hydrogen Energy **35**, 3919 (2010).
[25]M. Lessen, "On the stability of the free laminar boundary layer between parallel streams," Report No. NACA-TN-1929, 1949.
[26]C. Canuto, M. Y. Hussaini, A. Quarteroni, and T. A. Zang, *Spectral Methods in Fluid Dynamics* (Springer-Verlag, New York, 1988).
[27]R. L. Ash and M. R. Khorrami, in *Fluid Vortices*, edited by S. I. Green (Kluwer, Dordrecht, 1995), pp. 317–372.
[28]A. L. Sánchez, M. Vera, and A. Liñán, "Exact solutions for transient mixing of two gases of different densities," Phys. Fluids **18**, 078102 (2006).
[29]M. Abramowitz and I. A. Stegun, *Handbook of Mathematical Functions* (Dover, New York, 1965).
[30]H. Schlichting, "Laminare Strahlausbreitung," Z. Angew. Math. Mech. **13**, 260 (1933).
[31]H. Görtler. "Decay of swirl in an axially symmetrical jet far from the orifice," Rev. Mat. Hisp.-Am. **14**, 143 (1954).
[32]H. Schlichting, *Boundary Layer Theory*, 7th ed. (McGraw-Hill, New York, 1987).
[33]R. R. Long, "A vortex in an infinite viscous fluid," J. Fluid Mech. **11**, 611 (1961).
[34]A. Revuelta, A. L. Sánchez, and A. Liñán, "The virtual origin as a first-order correction for the far-field description of laminar jets," Phys. Fluids **14**, 1821 (2002).